The Structure and Dynamics of Tornado-Like Vortices

DAVID S. NOLAN*

Department of Mathematics, Lawrence Berkeley National Laboratory, Berkeley, California

BRIAN F. FARRELL

Department of Earth and Planetary Sciences, Harvard University, Cambridge, Massachusetts

(Manuscript received 24 November 1997, in final form 20 November 1998)

ABSTRACT

The structure and dynamics of axisymmetric tornado-like vortices are explored with a numerical model of axisymmetric incompressible flow based on recently developed numerical methods. The model is first shown to compare favorably with previous results and is then used to study the effects of varying the major parameters controlling the vortex: the strength of the convective forcing, the strength of the rotational forcing, and the magnitude of the model eddy viscosity. Dimensional analysis of the model problem indicates that the results must depend on only two dimensionless parameters. The natural choices for these two parameters are a convective Reynolds number (based on the velocity scale associated with the convective forcing) and a parameter analogous to the swirl ratio in laboratory models. However, by examining sets of simulations with different model parameters it is found that a dimensionless parameter known as the vortex Reynolds number, which is the ratio of the far-field circulation to the eddy viscosity, is more effective than the conventional swirl ratio for predicting the structure of the vortex.

As the value of the vortex Reynolds number is increased, it is observed that the tornado-like vortex transitions from a smooth, steady flow to one with quasiperiodic oscillations. These oscillations, when present, are caused by axisymmetric disturbances propagating down toward the surface from the upper part of the domain. Attempts to identify these oscillations with linear waves associated with the shears of the mean azimuthal and vertical winds give mixed results.

The parameter space defined by the choices for model parameters is further explored with large sets of numerical simulations. For much of this parameter space it is confirmed that the vortex structure and time-dependent behavior depend strongly on the vortex Reynolds number and only weakly on the convective Reynolds number. The authors also find that for higher convective Reynolds numbers, the maximum possible wind speed increases, and the rotational forcing necessary to achieve that wind speed decreases. Physical reasoning is used to explain this behavior, and implications for tornado dynamics are discussed.

1. Introduction

The use of numerical models has been one of the leading contributors to advances in our understanding of the causes and dynamics of the tornado phenomenon. This method of study can generally be divided into two categories: thunderstorm-scale simulations and tornado-scale simulations. In the former category, pioneered by Klemp and Wilhelmson (1978), three-dimensional cloud models are used to numerically simulate the formation and dynamics of the thunderstorms that are responsible for tornado formation. While the low resolution of such earlier models could only hope to simulate the thunderstorm-scale environment that is believed to lead to tornado formation, Wicker and Wilhelmson (1995) recently reported the simulation of tornado-like features within a numerically modeled thunderstorm. Tornado-scale models, pioneered by Rotunno (1977), assume a particular environment of rotation coupled with convection to create an intense vortex near the surface. These models are intended to provide the details of the wind field in the tornado and an understanding of the dynamics that lead to that flow structure. Until recently, most tornado-scale numerical models assumed the tornado to be axisymmetric, thereby reducing the problem from three dimensions to two dimensions in cylindrical coordinates.

Laboratory models, pioneered by Ward (1972), were the first to provide direct measurements of the wind field

* Current affiliation: Department of Atmospheric Science, Colorado State University, Fort Collins, Colorado.

Corresponding author address: Dr. David S. Nolan, Department of Atmospheric Science, Colorado State University, Fort Collins, CO 80523-1371.
E-mail: nolan@chandra.atmos.colostate.edu

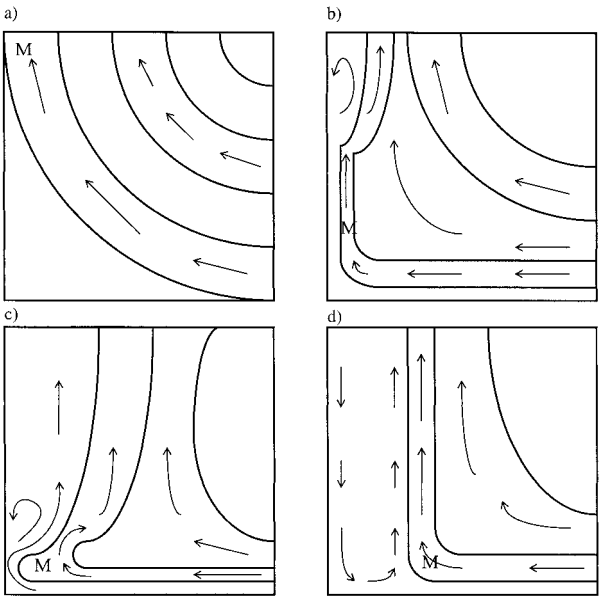

FIG. 1. Illustrations of four of the stages that laboratory and numerical models of tornados produce as the swirl ratio is increased from zero: (a) weak vortex stage; (b) surface vortex with vortex breakdown above the surface; (c) drowned vortex jump (breakdown just above the surface); and (d) two-celled vortex with stagnant core. The solid lines are streamlines of meridional flow, the arrows indicate the direction and details of the circulation, and the ''M'' marks the location of the maximum azimuthal (swirling) velocities.

associated with ''tornado-like'' vortices—a term that could apply to any vortex caused by the convergence of rotating fluid along a boundary. (These would also include waterspouts and dust devils, for example.) For this reason the early numerical modelers simulated the environment of the laboratory apparatus rather than that of a thunderstorm. That is, the numerically simulated vortex was driven by forcing rotating flow into the sides of the domain and drawing fluid out the top with some kind of outflow boundary conditions.

A significant result is that numerical models have been able to reproduce many of the features observed in laboratory vortices. The most universal feature of the laboratory results is the way in which the flow through the vortex depends on a nondimensional parameter known as the swirl ratio:

$$S = \frac{\Gamma r_0}{2Qh}, \tag{1.1}$$

where Γ is the circulation of the air as it enters the convection region in the apparatus, r_0 is the radius of the updraft, Q is the volume flow rate per unit axial length, and h is the depth of the inflow region (Church et al. 1979). As the value of the swirl ratio is increased, the vortex goes through various stages, as depicted in Fig. 1. For $S < 0.1$, there is no concentrated vortex at the surface. For larger values, a concentrated vortex does appear at the surface, and at some height above it there is a ''vortex breakdown'' where the flow transitions from a tight, laminar vortex to a broader, turbulent state. The vortex breakdown (Harvey 1962; Benjamin 1962; Lugt 1989) is considered to be an axisymmetric analog to the hydraulic jump phenomenon observed in channel flows. As S is increased, the altitude of the vortex breakdown decreases; until around $S = 0.45$ the breakdown is just above the surface (Church et al. 1979; Church and Snow 1993). This state has been referred to as a ''drowned vortex jump'' (DVJ; Maxworthy 1973) and is generally associated with having the highest near-surface azimuthal wind velocities. (This value of S for the DVJ was found for the Ward vortex chamber and may be different for other physical models.) When S is further increased, the vortex breakdown reaches the surface and the vortex changes to a ''two-celled'' structure, where there is a downward recirculation in the vortex core and the radius of maximum winds substantially increases. Still larger values of S result in the appearance of multiple vortices rotating around the vortex core. These values of S did have some dependence on the Reynolds number (Re, as measured by the volume flow rate through the chamber), but this dependency decreases for increasing Re. Three-dimensional models have also reproduced this multiple vortex phenomenon (Rotunno 1984; Lewellen 1993). A general review of laboratory modeling of tornado-like vortices can be found in Church and Snow (1993).

Wilson and Rotunno (1986) used a model based on earlier work by Rotunno (1979, 1984) to address the validity of various approximate laminar solutions for swirling boundary layers. They found good agreement with those solutions and with laboratory results. Howells et al. (1988) focused instead on the dynamics over a wide range of swirl ratios and eddy viscosities and studied the effect of no-slip versus free-slip lower boundary conditions. Their results demonstrated that the combination of high swirl ratio, low eddy viscosity, and the no-slip boundary conditions produced the highest near-surface wind speeds. This combination (low viscosity but no-slip boundary conditions) may be counterintuitive at first, but what Howells et al. (1988) demonstrated was the importance of a thin but strong inward jet at the surface that, in the no-slip case, drives the fluid above the jet much closer to $r = 0$ than is possible with free-slip conditions.

More recent efforts to study tornadic vortices with an axisymmetric model have been made by Fiedler (1993, 1994, 1995; hereafter F93, F94, F95, respectively) whose motivation was to determine the maximum velocities that a tornado-like vortex could achieve as compared to the velocity associated with the ''thermodynamic speed limit'' (Lilly 1969; Fiedler and Rotunno 1986). This estimated speed limit is made by matching the minimum surface pressure, calculated from hydrostatic integration of the overhead density profile, with the central pressure deficit of a Rankine vortex or some other vortex profile. For a Rankine vortex, which has solid-body rotation $v = v_{\max} r/r_{\max}$ out to some radius

r_{max}, and a potential flow $v = v_{max} r_{max}/r$ outside of $r = r_{max}$, the pressure deficit Δp_{cyc} at $r = 0$ due to cyclostrophic balance must be

$$\begin{aligned}\Delta p_{cyc} &= -\int_0^{\infty} \rho \frac{v^2}{r}\, dr \\ &= -\int_0^{r_{max}} \rho \frac{v_{max}^2}{r_{max}^2} r\, dr - \int_{r_{max}}^{\infty} \rho v_{max}^2 r_{max}^2 \frac{1}{r^3}\, dr \\ &= -\rho v_{max}^2, \end{aligned} \tag{1.2}$$

where ρ is the air density. Note that the size of the vortex, as indicated by r_{max}, does not appear in the result. The hydrostatic pressure deficit beneath a convecting updraft may be computed from the overhead density profile of the updraft column:

$$\Delta p_{hyd} = \int_0^{\infty} \rho' g\, dz = -\int_0^{\infty} \rho g \frac{T'}{T}\, dz, \tag{1.3}$$

where ρ' and T' are the density and temperature deviations in the updraft from the ambient temperature ρ and T, and we have used the Boussinesq approximation. The assumption that the minimum pressure achievable in the vortex is due entirely to this hydrostatic pressure deficit gives the thermodynamic speed limit:

$$\Delta p_{hyd} = C \rho v_{max}^2, \tag{1.4}$$

where C is some constant that depends on the vortex profile. For a Rankine vortex, $C = 1.0$; $C = 0.5$ for a stagnant core vortex [this can be seen by neglecting the integral from 0 to r_{max} in (1.2)]; and $C = 0.59$ for a Burgers's vortex velocity profile. F93–95 used a closed cylindrical domain, which has the advantage of preventing inflow–outflow boundary conditions from contributing to the energetics of the model. (Previous numerical models used fixed inflow or outflow velocities, which can act as variable energy sources.) Rather than modeling the temperature of the fluid, Fiedler used a fixed buoyancy field at the center axis of the domain to convectively drive the flow and force convergence at the lower boundary. Angular momentum was supplied by putting the entire domain into solid-body rotation. F93 and F94 explored the effects of the choice of rotation rate, eddy viscosity, and also the additional effect of subsidence warming in the core on the maximum wind speeds. Based on the assumption that the pressure deficit of a drowned vortex jump can be approximated by that of a stagnant-core vortex, F94 observed transient vortices that exceed the thermodynamic speed limit by a factor of 5. These very high transient wind speeds remind us that there is nothing about the concept or derivation of the thermodynamic speed limit that proves that it is a real constraint on the maximum velocities that can be generated in a convectively driven vortex. This is because the hydrostatic and cyclostrophic assumptions are clearly violated in the presence of substantial vertical and horizontal accelerations. Lewellen (1993) wrote, ''The tornado vortex allows a significant fraction of the potential energy of the parent storm to be concentrated into wind kinetic energy where it can cause great damage.'' How exactly this occurs is still a matter of investigation.

The results of axisymmetric tornado-like vortex models have been strongly confirmed by the first detailed observations of the tornado vortex core reported by Wurman et al. (1996) using the most recent advances in Doppler radar technology. Their observations of a tornado near Dimmit, Texas, during the VORTEX field program (Rasmussen et al. 1994) showed maximum wind speeds of over 70 m s^{-1} occurring less than 200 m above the ground in a tight ring around the center of the tornado. The structure of the azimuthal wind field they observed was very consistent with those generated by the simulations of Howells et al. (1988), F93 and F94, and also with the results we are about to show.

In this study we will examine not only the maximum wind speeds of axisymmetric tornado-like vortices, but also how the major model parameters—the buoyancy forcing, the rotational forcing, and the eddy viscosity—determine these wind speeds as well as the structure and behavior of the vortex. In section 2 we introduce the equations of motion and our methods of numerical integration. In section 3 we show the basic features of the simulated vortices and we introduce a way to measure the relative values of the azimuthal and vertical wind speeds in the vortex core, which is analogous to the swirl ratio (1.1). In section 4 we discuss the dimensionless parameters that control the flow. In section 5 we investigate how the structure and behavior of the flow in the vortex depend on these dimensionless parameters. In section 6 we give some analysis of the results, and in section 7 we discuss their implications.

2. Numerical modeling of the axisymmetric Navier–Stokes equations

a. The equations of motion and nondimensionalization

The incompressible Navier–Stokes equations for a constant-density, constant-viscosity fluid in cylindrical coordinates, with all azimuthally varying terms eliminated, are

$$\frac{\partial u}{\partial t} + u\frac{\partial u}{\partial r} + w\frac{\partial u}{\partial z} - \frac{v^2}{r} = -\frac{1}{\rho}\frac{\partial p}{\partial r} + \frac{\mu}{\rho}\left[\frac{\partial}{\partial r}\left(\frac{1}{r}\frac{\partial}{\partial r}(ru)\right) + \frac{\partial^2 u}{\partial z^2}\right] \tag{2.1}$$

$$\frac{\partial v}{\partial t} + u\frac{\partial v}{\partial r} + w\frac{\partial v}{\partial z} + \frac{uv}{r} = \frac{\mu}{\rho}\left[\frac{\partial}{\partial r}\left(\frac{1}{r}\frac{\partial}{\partial r}(rv)\right) + \frac{\partial^2 v}{\partial z^2}\right] \tag{2.2}$$

$$\frac{\partial w}{\partial t} + u\frac{\partial w}{\partial r} + w\frac{\partial w}{\partial z} = -\frac{1}{\rho}\frac{\partial p}{\partial z} + \frac{\mu}{\rho}\left[\frac{1}{r}\frac{\partial}{\partial r}\left(r\frac{\partial w}{\partial r}\right) + \frac{\partial^2 w}{\partial z^2}\right] + F_z \tag{2.3}$$

$$\frac{1}{r}\frac{\partial}{\partial r}(ru) + \frac{\partial w}{\partial z} = \frac{\partial u}{\partial r} + \frac{u}{r} + \frac{\partial w}{\partial z} = 0, \tag{2.4}$$

where u is the radial velocity, v is the azimuthal velocity, w is the vertical velocity, p is the pressure, F_z is a vertical forcing term (the buoyant acceleration), μ is the viscosity, and band ρ is the density. Equation (2.4) is the incompressibility condition for axisymmetric flow.

The variables in (2.1)–(2.4) are nondimensionalized as follows:

$$(u, v, w) = U(u', v', w') \tag{2.5}$$

$$(r, z) = L(r', z') \tag{2.6}$$

$$p = Pp' \tag{2.7}$$

$$F_z = FF_z' \tag{2.8}$$

$$t = Tt' = \left(\frac{L}{U}\right)t', \tag{2.9}$$

where nondimensional variables are indicated by primes, and we have used an advective timescale in (2.9). For the moment we will postpone selection of the magnitudes of the dimensional parameters U, L, P, and F. Substitution of the scalings (2.5)–(2.9) into the momentum equations (2.1)–(2.3) results in the usual nondimensionalization of the Navier–Stokes equations, with $\mu/\rho UL = 1/\mathrm{Re}$ (the inverse Reynolds number) multiplying the diffusion terms, $P/\rho U^2$ multiplying the pressure gradient terms, and the nondimensional parameter FL/U^2 multiplying the vertical forcing term F_z'.

Following F93, we scale the velocities according to the thermodynamic speed limit (1.4). We choose the length scale to be the height of the domain, the forcing scale F to be the average of the dimensional forcing along the $r = 0$ axis, $F = \langle F_z(0, z)\rangle$, and

$$U^2 = FL \tag{2.10}$$

$$P = \rho FL \tag{2.11}$$

$$\nu = \frac{\mu}{\rho UL} = \frac{1}{\mathrm{Re}}. \tag{2.12}$$

Using these scalings, and dropping the primes on the nondimensional variables, we obtain the nondimensional equations of motion:

$$\frac{\partial u}{\partial t} + u\frac{\partial u}{\partial r} + w\frac{\partial u}{\partial z} - \frac{v^2}{r} = -\frac{\partial p}{\partial r} + \nu\left[\frac{\partial}{\partial r}\left(\frac{1}{r}\frac{\partial}{\partial r}(ru)\right) + \frac{\partial^2 u}{\partial z^2}\right] \tag{2.13}$$

$$\frac{\partial v}{\partial t} + u\frac{\partial v}{\partial r} + w\frac{\partial v}{\partial z} + \frac{uv}{r} = \nu\left[\frac{\partial}{\partial r}\left(\frac{1}{r}\frac{\partial}{\partial r}(rv)\right) + \frac{\partial^2 v}{\partial z^2}\right] \tag{2.14}$$

$$\frac{\partial w}{\partial t} + u\frac{\partial w}{\partial r} + w\frac{\partial w}{\partial z} = -\frac{\partial p}{\partial z} + \nu\left[\frac{1}{r}\frac{\partial}{\partial r}\left(r\frac{\partial w}{\partial r}\right) + \frac{\partial^2 w}{\partial z^2}\right] + F_z \tag{2.15}$$

$$\frac{1}{r}\frac{\partial}{\partial r}(ru) + \frac{\partial w}{\partial z} = \frac{\partial u}{\partial r} + \frac{u}{r} + \frac{\partial w}{\partial z} = 0. \tag{2.16}$$

b. *Numerical integration of the Navier–Stokes equations*

There are two computational challenges to numerical modeling of the equations of motion. The first is the enforcement of incompressibility (2.16); the second is the evaluation of the nonlinear advection terms in the momentum equations (2.13)–(2.15) in a manner that is accurate and keeps the solution stable. Traditional methods (Rotunno 1979; F93) have used the following techniques for these problems. First, the radial and vertical momentum equations are combined into a streamfunction-vorticity equation and the pressure is thereby eliminated from the problem. This, however, creates the need to calculate the streamfunction from the vorticity, which has many challenges, particularly the extrapolation of the (unknown) vorticity to the domain boundaries. Second, the nonlinear terms in the streamfunction-vorticity equation are computed from an Arakawa-type Jacobian, which keeps the system stable as long as the usual time step constraints are met.

We have instead used a velocity–pressure formulation. First, we consider the equations of motion as a simplified vector equation:

$$\frac{\partial \mathbf{u}}{\partial t} = \mathbf{F}(\mathbf{u}) - \nabla p. \tag{2.17}$$

Here we have written the functional $\mathbf{F}(\mathbf{u})$ in place of the advective, diffusive, and vertical forcing terms. Since $\mathbf{u}$ is always nondivergent, so must be $\partial\mathbf{u}/\partial t$. We also know that an arbitrary vector field, such as one generated by $\mathbf{F}(\mathbf{u})$, can be written as the sum of a nondivergent part and an irrotational (and divergent) part, the uniqueness of which is provided by the boundary conditions. Therefore, we can conclude that for $\mathbf{u}$ to remain nondivergent, $-\nabla p$ must exactly cancel the irrotational part of $\mathbf{F}(\mathbf{u})$. Suppose we had some method for directly extracting the nondivergent part of $\mathbf{F}(\mathbf{u})$. We call this the projection $\mathbf{P}$ of $\mathbf{F}(\mathbf{u})$ onto the space of divergence-free vector fields. The equations of motion can then be succinctly written as $\partial\mathbf{u}/\partial t = \mathbf{P}[\mathbf{F}(\mathbf{u})]$. The theory and technique behind this method were introduced by Chorin (1968, 1969) and have been developed extensively since then (see, e.g., the text by Peyret and Taylor 1983). Most recent projection methods are second-order accurate in space and time. In axisymmetric flows the swirling velocity v is already nondivergent and is left out of the projection.

For the nonlinear advection terms, we used a Godunov-type upwinding method developed by Colella (1990) and Bell et al. (1989) that is also second-order accurate. This method approximately solves the Riemann problem in the vicinity of each grid point and ultimately becomes a fully explicit approximation to a Crank–Nicholson method. The interested reader may find more details in Minion (1994, 1996).

In this model, the domain is divided into rectangular cells, with velocity information stored at the cell centers

and the scalar information stored at the cell corners. The edges of the outermost cells are coincident with the domain boundaries. All the simulations reported here use grids that are regularly spaced in each direction, with 64 × 64 grid points, 128 × 128 grid points, and, in one case, 256 × 128 grid points. A complete description of this axisymmetric incompressible numerical model may be found in Nolan (1996).

3. Preliminary results

a. Comparison to previously reported results

We tested the model by comparing it to some previously published results, using the same type of domain, boundary conditions, and forcing. As discussed above, F93 used an axisymmetric incompressible flow model to investigate the dynamics of vortices generated by convection in a rotating domain. He used the streamfunction-vorticity method and modified the equations so that the domain was in solid-body rotation at a dimensionless rotation rate $\Omega = 0.2$. The simulations were nondimensional, with a domain height of $Z = 1$ and radius of $R = 2$. This radius was chosen to be large enough so as not to influence the behavior of the vortex near $r = 0$. Although our equations did not have a Coriolis term to represent solid-body rotation, we were able to reproduce the F93 results by initializing the azimuthal velocity with $v = \Omega r$ and setting the boundaries in rotation at the same rate. We used the F93 buoyancy field:

$$F_z(r, z) = 1.264e^{-20[r^2+(z-0.5)^2]}. \quad (3.1)$$

Finally, we also begin with the same value for the nondimensional kinematic viscosity (the inverse Reynolds number) $\nu = 0.0005$. The major and nonreproducible difference between the F93 simulations and ours is that F93 used a stretched coordinate system that packed the grid points near $r = 0, z = 0$, whereas ours was designed such that it could only have equal gridpoint separation in each direction. F93 used 61 × 61 (stretched) grid points for most of his simulations, whereas we use 128 × 128 in this case.

Figure 2 shows the vertical velocities, azimuthal velocities, pressure, and the velocity vectors in the r–z plane at $t = 10$ for a simulation based on the F93 conditions. The velocity vectors in the r–z plane are hereafter referred to as the meridional velocity vectors. Figure 3 shows these fields at $t = 40$. (Note that these times were chosen so that our results can be compared with those of F93; however, one must also note that we are plotting v, which includes the rotation of the domain, while F93 did not. Since Ωr is small near $r = 0$, the results are nearly identical in the vortex core.) At $t = 40$ we can see in the meridional vector velocity plot how the vertical flow in the vortex core separates from the $r = 0$ axis, and we can also see in the vertical velocity contour plot the appearance of a recirculation zone above the vortex core, as indicated by the negative velocities just above the surface. This feature is generally interpreted to be an axisymmetric equivalent of the vortex breakdown seen in the laboratory experiments (cf. Fig. 1). The maximum velocities and minimum pressure occurring in the domain as a function of time are shown in Fig. 4. This pressure is purely dynamic and is defined to be zero in the upper-right-hand corner of the domain. One can see a pattern where all three velocities episodically increase and then decrease in time. Longer simulations (not shown) revealed that these oscillations in the maximum velocities did not decay completely but periodically reappeared for as long as the simulation with these parameters was integrated. The cause of these oscillations will be discussed further below in section 6. We found that the similarity of our results to F93 was qualitatively very high, while quantitatively they were fairly similar, although there are significant differences in the maximum velocities. Our maximum azimuthal velocity is $v_{\max} = 1.16$, which occurs at $t = 11.6$; for F93, the result was $v_{\max} = 1.26$ at time $t = 11$.

By comparing the maximum velocities at $t = 10$ and $t = 40$, we are inclined to draw the conclusion that the vortex is much stronger during its intensification stage than when it has settled into a nearly steady state. For certain values of rotation rate and eddy viscosity, F94 observed transient maximum wind speeds as much as five times faster than the thermodynamic speed limit defined by the stagnant-core vortex. However, it is not likely that these transient solutions offer much guidance to the dynamics of real tornadoes, which certainly do not form when a fixed vertical forcing field is instantaneously applied to a column of air in solid-body rotation. Furthermore, since tornadoes have been observed to produce damaging winds for as long as 45 minutes, it is a quasi-steady-state solution that should represent them best. With this in mind, our goal should be to focus on the dynamics of quasi-steady solutions.[1]

b. The effect of the ceiling at z = 1

It is reasonable to wonder to what extent the ''ceiling'' at $z = 1$ effects the formation and behavior of the vortex at the lower surface. One may also speculate that the recirculation seen in the fully developed vortex owes its existence, at least in part, to the ceiling. To address these concerns, we ran another simulation with the same grid spacing but twice the domain size in the vertical

[1] Note added in proof: Observations and numerical simulations indicate that the highest transient wind speeds in tornadoes occur in secondary vortices, which appear episodically in the region of large shear just inside the radius of maximum winds. In fairness, then, it is likely that Fielder's (1994) study of the very high transcient wind speeds that occur in the early development of tornado-like vortices is applicable to these secondary vortices.

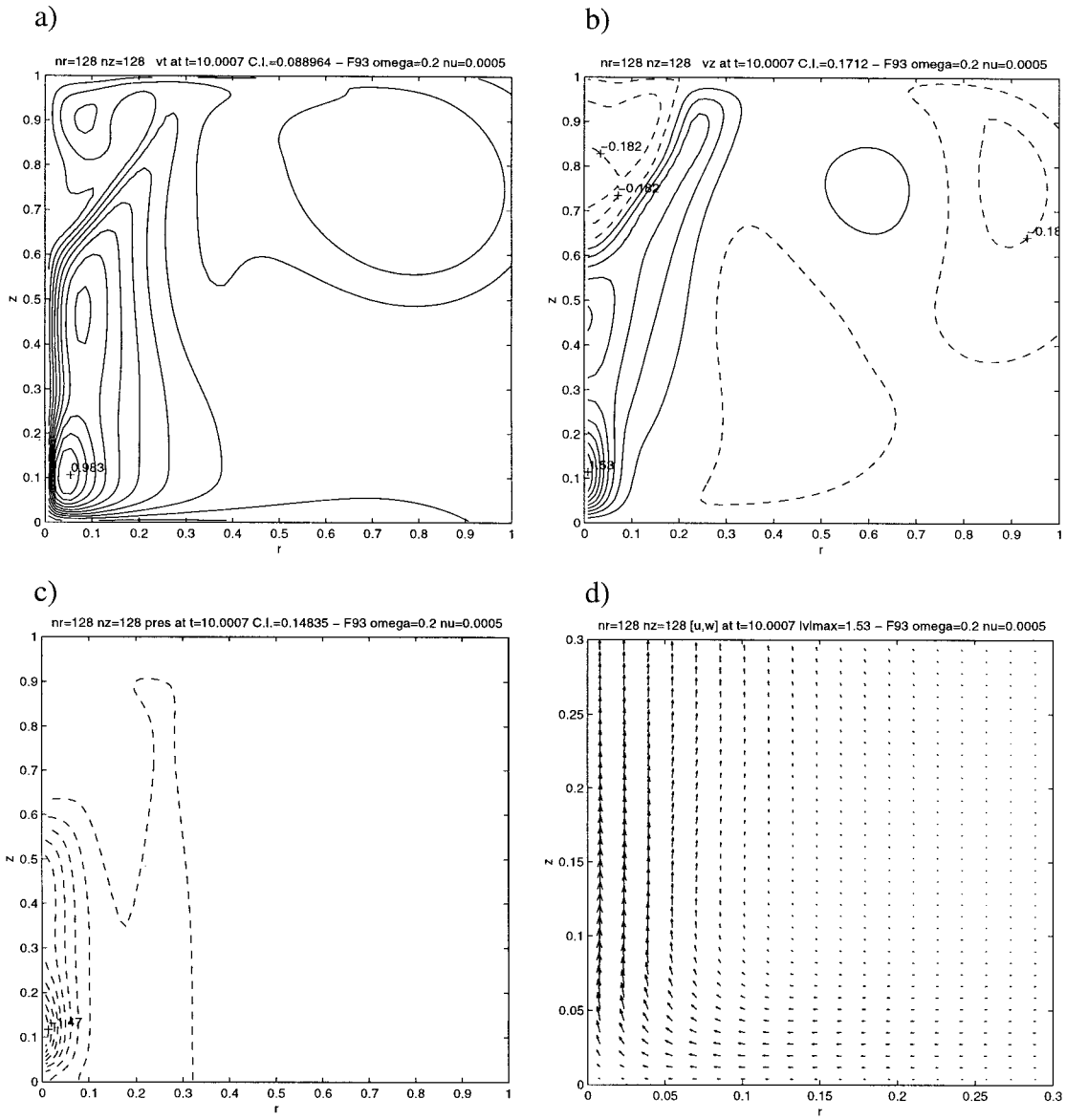

FIG. 2. Results for the F93-type simulation at $t = 10$: (a) swirling (azimuthal) velocity; (b) vertical velocity; (c) pressure; and (d) meridional velocity vectors in the r–z plane. Dashed contours indicate negative values, maxima and minima are indicated, and the contour intervals are indicated at the top of each plot. All plots show the domain for $0 < r < 1$, $0 < z < 1$, except for the meridional vector velocity plot, which is for $0 < r < 0.3$, $0 < z < 0.3$.

direction; this required using 256 grid points in the vertical direction. The results are shown in Fig. 5 for the azimuthal and vertical velocities at $t = 10$ and $t = 40$. Comparing these to the previous results at $t = 10$ and $t = 40$, as shown in Figs. 2 and 3, we see that the results with a higher ceiling are very similar. Note especially the appearance of a recirculation zone above the fully developed drowned vortex jump vortex at $t = 40$. This vortex is slightly different in that this recirculation zone is slightly weaker and the maximum azimuthal wind speeds are slightly higher. However, the overall results are essentially the same.

c. *Three measured parameters to characterize the vortex*

As discussed in section 1, laboratory modelers found a correlation between the structure of the tornado-like vortex and the value of the nondimensional swirl ratio S as defined by (1.1). This swirl ratio depends on the

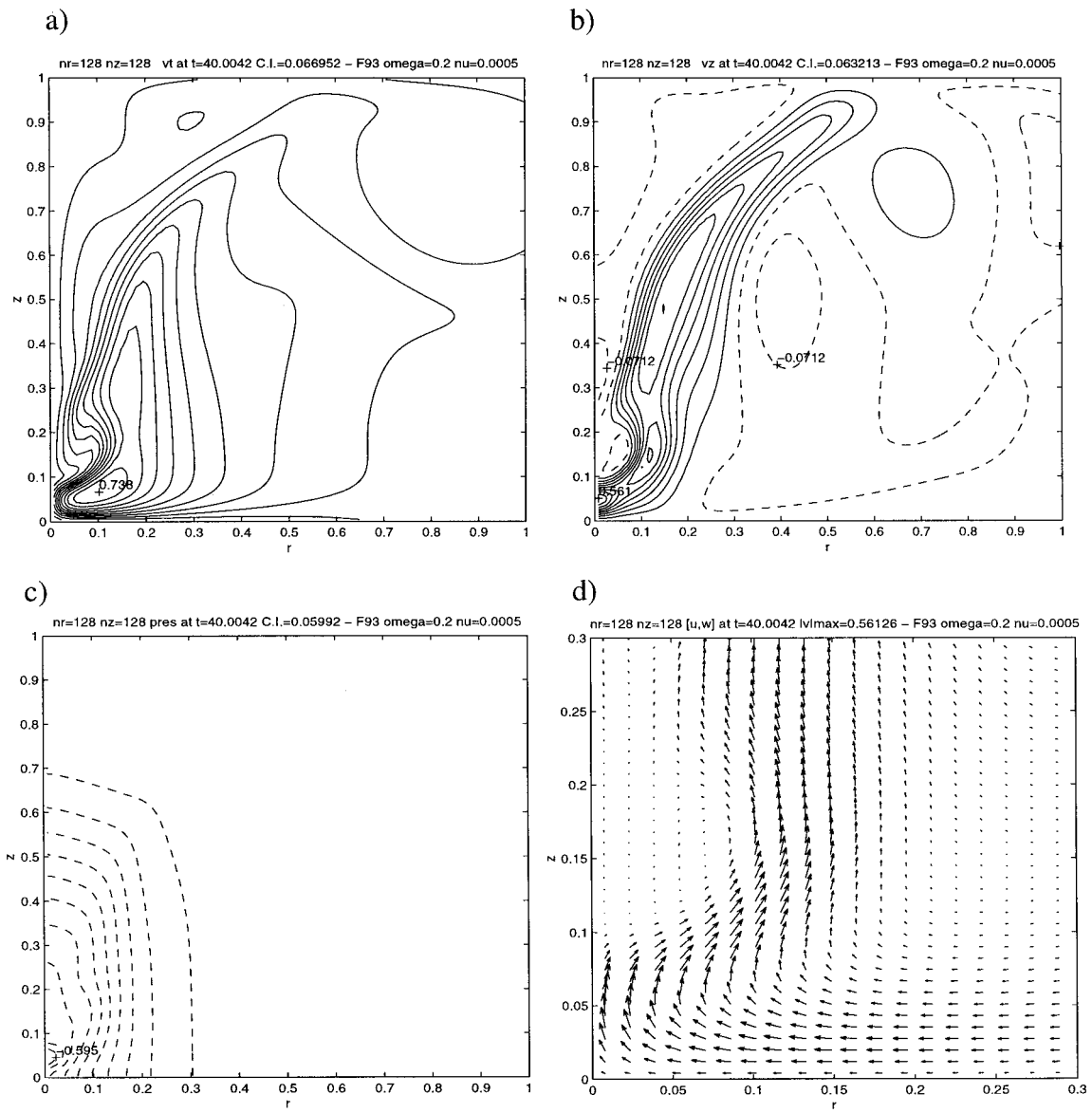

FIG. 3. Results for the F93-type simulation at $t = 40$: (a) swirling (azimuthal) velocity; (b) vertical velocity; (c) pressure; and (d) meridional velocity vectors in the r–z plane. Dashed contours indicate negative values, maxima and minima are indicated, and the contour intervals are indicated at the top of each plot. All plots show the domain for $0 < r < 1$, $0 < z < 1$, except for the meridional vector velocity plot, which is for $0 < r < 0.3$, $0 < z < 0.3$.

volume flow rate of the air through the apparatus and its required rotation rate as it enters the convection zone. The conventional definition of the swirl ratio is not applicable to closed domain models such as ours and that of F93, because the rotation and flow rates of the fluid through the central vortex is not under the control of the modeler. However, we can instead define an ''internal'' swirl ratio based on the measured rotation and flow rates of the fluid through the region surrounding the vortex. To do this, we define a control volume that surrounds the central vortex, such that the boundaries of the control volume represent the inflow region into the vortex, the outflow region above the vortex, the surface, and $r = 0$. We define the *internal swirl ratio* S_I as

$$S_I \equiv \frac{r_0}{2h_0} \frac{\int_0^{h_0} \Gamma(r_0, z)\, dz}{\int_0^{r_0} w(r, z_0) 2\pi r\, dr}, \tag{3.2}$$

where Γ is the circulation $2\pi rV$. For our simulations here we use $r_0 = 0.25$ and $h_0 = 0.25$, so that the control

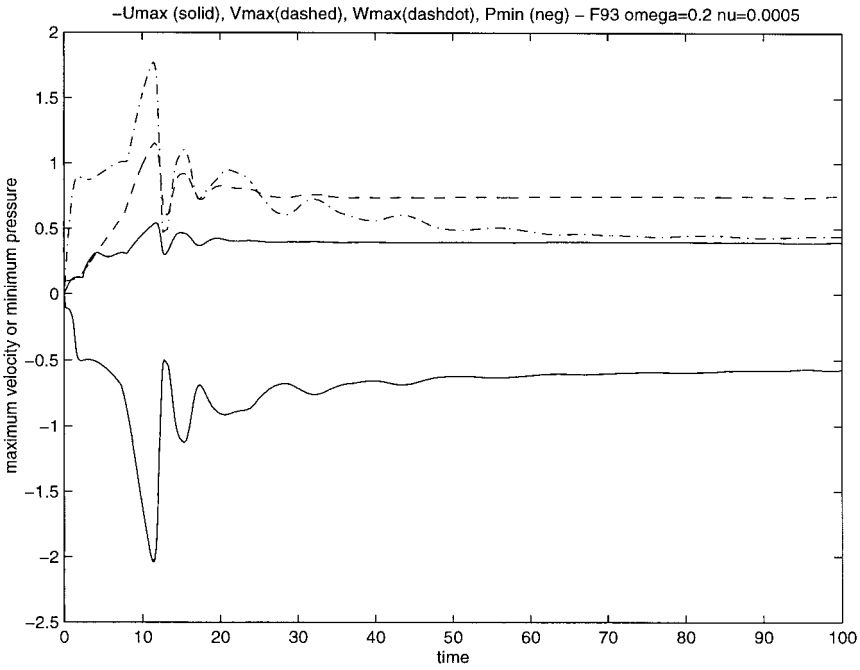

FIG. 4. Maximum velocities and minimum pressure as a function of time in the original F93-type simulation: vertical velocity (dash–dot), azimuthal velocity (dashed), inward radial velocity (solid), and pressure (solid, negative).

volume is a cylinder of radius 0.25 and depth 0.25, adjacent to the corner at $r = 0$, $z = 0$.

We shall now introduce another parameter that characterizes the flow. Recall that the motivation for F93 and F94 was to determine the maximum wind speeds that can be generated by a given buoyancy field. The vertical integral along $r = 0$ of the buoyancy function (3.1) was considered to be analogous to convective available potential energy (CAPE), which is a way of expressing the potential intensity of thunderstorms from their environmental thermodynamic sounding (Emanuel 1994). Note also that when the background vertical density profile is constant, the CAPE is equal to the potential minimum hydrostatic pressure divided by the density ρ, that is,

$$\text{CAPE} = \int_0^{\text{LNB}} g\frac{\delta T'}{T}\,dz = -\frac{\Delta p_{\text{hyd}}}{\rho}, \qquad (3.3)$$

where LNB is the level of neutral buoyancy and $\delta T'(z)$ is the temperature deviation from the background temperature $T(z)$ of a parcel of air rising adiabatically from the surface to the LNB. The maximum integral of force time distance [integral of $b(0, z)$] for the forcing field (3.1) is 0.5; this is the ''CAPE'' for our model. F93 and F94 argued that the drowned vortex jump state has a cyclostrophic pressure drop that is similar to that of a stagnant-core vortex that has $C = 0.5$, so the thermodynamic speed limit was therefore $v_{\max} = 1$. Even when the vortex is not in hydrostatic balance, we expect from dimensional considerations that the square of the maximum azimuthal velocity would be proportional to the equivalent of the CAPE for our numerical model:

$$\int_0^1 b(0, z)\,dz = Cv_{\max}^2, \qquad (3.4)$$

where C is some coefficient that may also depend on the viscosity and the rotational forcing. As discussed in section 1, this coefficient has certain well-known values for various idealized velocity profiles. However, this C is not so easily interpreted since, for a given convective forcing, it is proportional to the inverse of the square of the maximum azimuthal velocity. Let us define a new *velocity coefficient*, C_v, as

$$C_v \equiv \frac{v_{\max}}{\left(2\int_0^1 b(0, z)\,dz\right)^{1/2}} = \frac{v_{\max}}{w_{\text{CAPE}}}, \qquad (3.5)$$

so that C_v is the ratio of the maximum swirling velocity to the maximum convective velocity predicted from the CAPE equivalent.

Figure 6 shows the internal swirl ratio S_I and the velocity coefficient C_v during the original F93-type simulation described above. Initially S_I is not well defined since no meridional flow exists at $t = 0$; however, as the vortex forms it quickly adjusts to appropriate values. Around $t = 10$, S_I wildly oscillates around a value of approximately 2.5 in a manner similar to the maximum vertical velocities (see Fig. 4); as the vortex settles into a quasi-steady state these oscillations persist with much

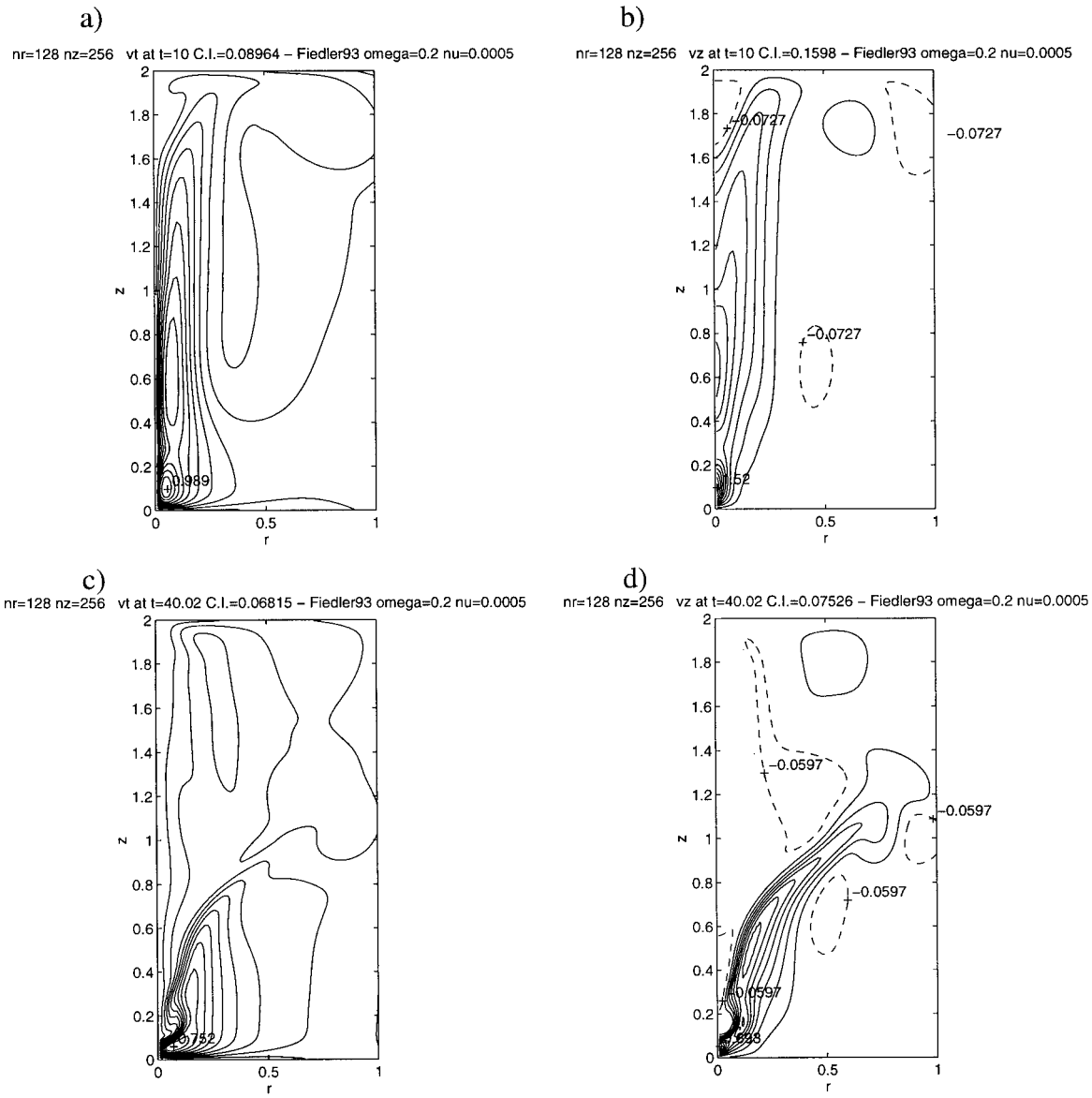

FIG. 5. Results of an F93-type simulation with twice the domain height: (a) contours of azimuthal velocity at $t = 10$; (b) contours of vertical velocity at $t = 10$; (c) contours of azimuthal velocity at $t = 40$; and (d) contours of vertical velocity at $t = 40$. The domain in each frame is from $0 < r < 1$, $0 < z < 2$. Dashed contours indicate negative values, maxima and minima are indicated, and the contour intervals are indicated at the top of each plot.

smaller magnitudes and a seemingly constant frequency. Around $t = 10$, C_v shows large oscillations about a value of 0.7 but then settles into a nearly constant value of 0.8. This constancy is in contrast to the oscillations in S_I, and it indicates that even while the ratio of the volumetric flow through the vortex core to the angular momentum entering the vortex core may be varying in time, the maximum azimuthal wind speed is nearly constant.

The internal swirl ratio S_I depends explicitly on the choice for the dimensions of the control volume defined above, and has been found to have higher values for larger control volumes and lower values for smaller control volumes. Unfortunately, then, the internal swirl ratio is not universal and cannot be compared to the swirl ratios measured in laboratory models. An alternative way to evaluate the structure of the flow in the vortex core is to introduce the *vortex aspect ratio*, A_V, which is the ratio of the radius of the location of the maximum azimuthal wind speed (RMW) to the height of the location of the maximum azimuthal wind speed (ZMW):

$$A_V = \frac{\text{RMW}}{\text{ZMW}}. \tag{3.6}$$

With the recent arrival of finescale Doppler radar mea-

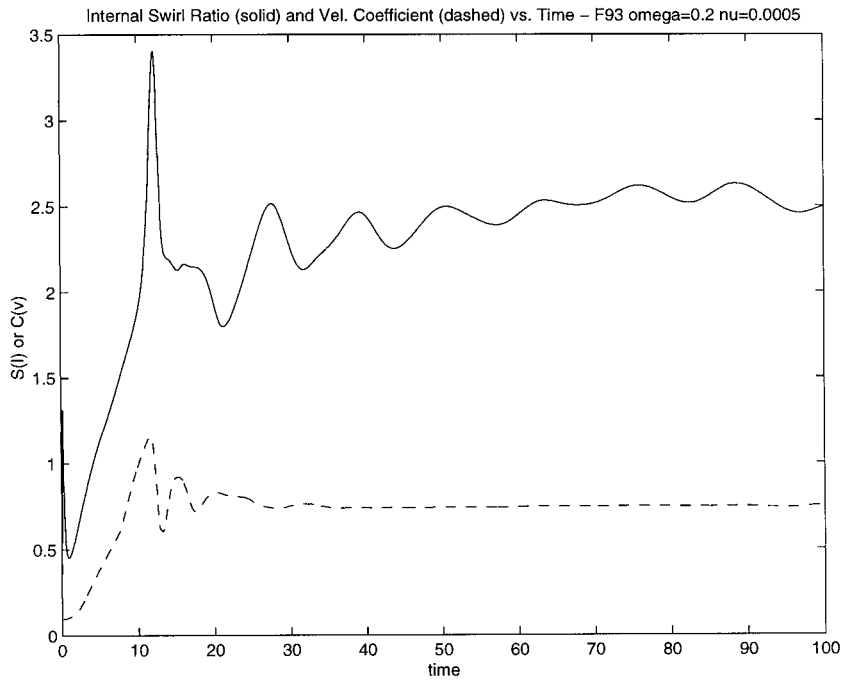

FIG. 6. Internal swirl ratio S_I (solid line) and velocity coefficient C_v (dashed lined) during the F93-type simulation shown above.

surements of tornadic wind fields (Wurman et al. 1996) this parameter can be measured quite accurately in real tornadoes, since the actual values of RMW and ZMW do not need to be measured—just their ratio. The time evolution of A_V for the F93 simulation is shown in Fig. 7. While A_V is clearly meaningless until an intense vortex forms near the axis, it does reflect the structure of the vortex as it evolves: first it has low values around

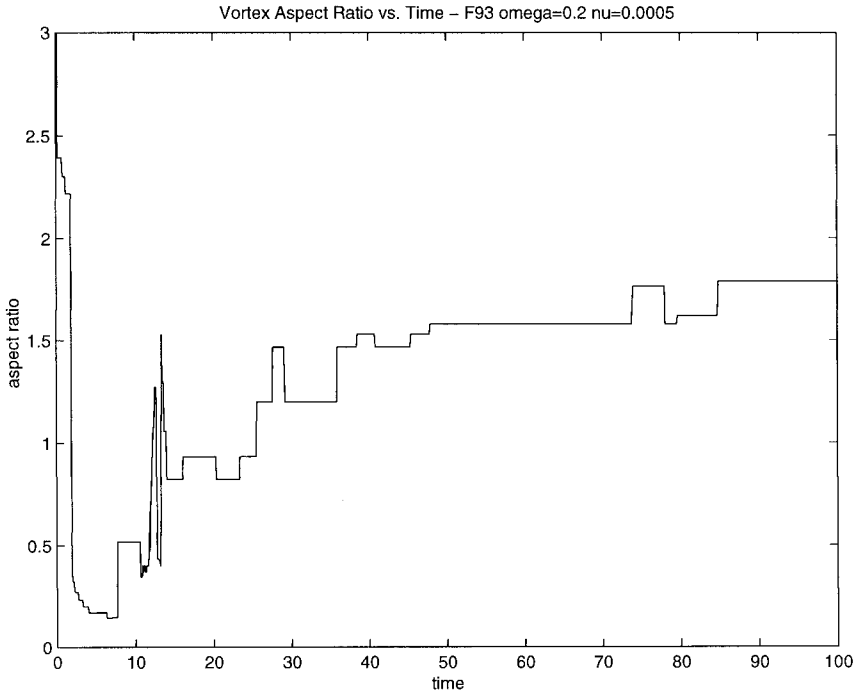

FIG. 7. Vortex aspect ratio (RWM/ZMW) as a function of time in the F93 simulation.

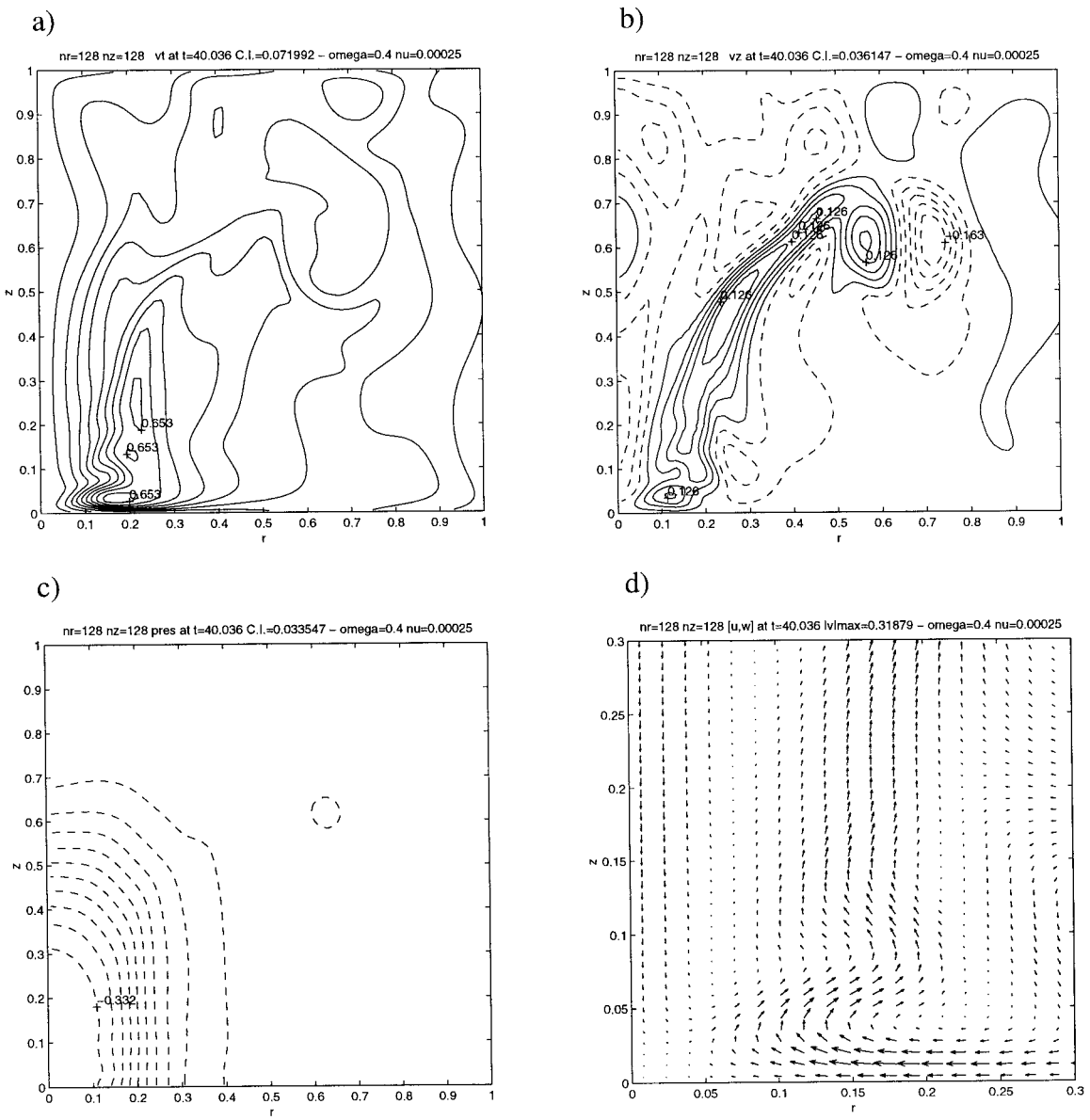

FIG. 8. Results for a simulation with $\Omega = 0.4$ and $\nu = 0.00025$ at $t = 40$: (a) swirling (azimuthal) velocity; (b) vertical velocity; (c) pressure; and (d) meridional velocity vectors in the r–z plane. Dashed contours indicate negative values, maxima and minima are indicated, and the contour intervals are indicated at the top of each plot. All plots show the domain for $0 < r < 1$, $0 < z < 1$, except for the meridional vector velocity plot, which is for $0 < r < 0.3$, $0 < z < 0.3$.

0.5 when the vortex is of the ''end-wall'' type, then goes through some wild oscillations as the breakdown appears, and finally settles down to small oscillations around a value of 1.8 as the drowned vortex jump stabilizes. Figure 7 does show one of the limitations of A_V as we have defined it: since the numerical model stores velocities at discrete locations, the locations of the velocity maxima are discrete, so we see that A_V goes through discontinous jumps between discrete values as time evolves. This should be contrasted with the very smooth behavior of S_I (see Fig. 6).

To show how these measured parameters depend on the structure of the vortex, we consider the results of a simulation with Ω increased to 0.4 and ν decreased to 0.00025. These values of Ω and ν result in a vortex that oscillates chaotically between a drowned vortex jump and a two-celled vortex. An example of the flow field when the vortex is in a two-celled state is shown in Fig. 8. There is a recirculation zone in the core of the vortex, with downward flow penetrating all the way to the surface. The maximum azimuthal winds are farther out from the axis and closer to the surface. Figure 9 shows S_I, C_v, and A_V as a function of time for this simulation. Comparison of Fig. 9 with Fig. 6 shows the strengths

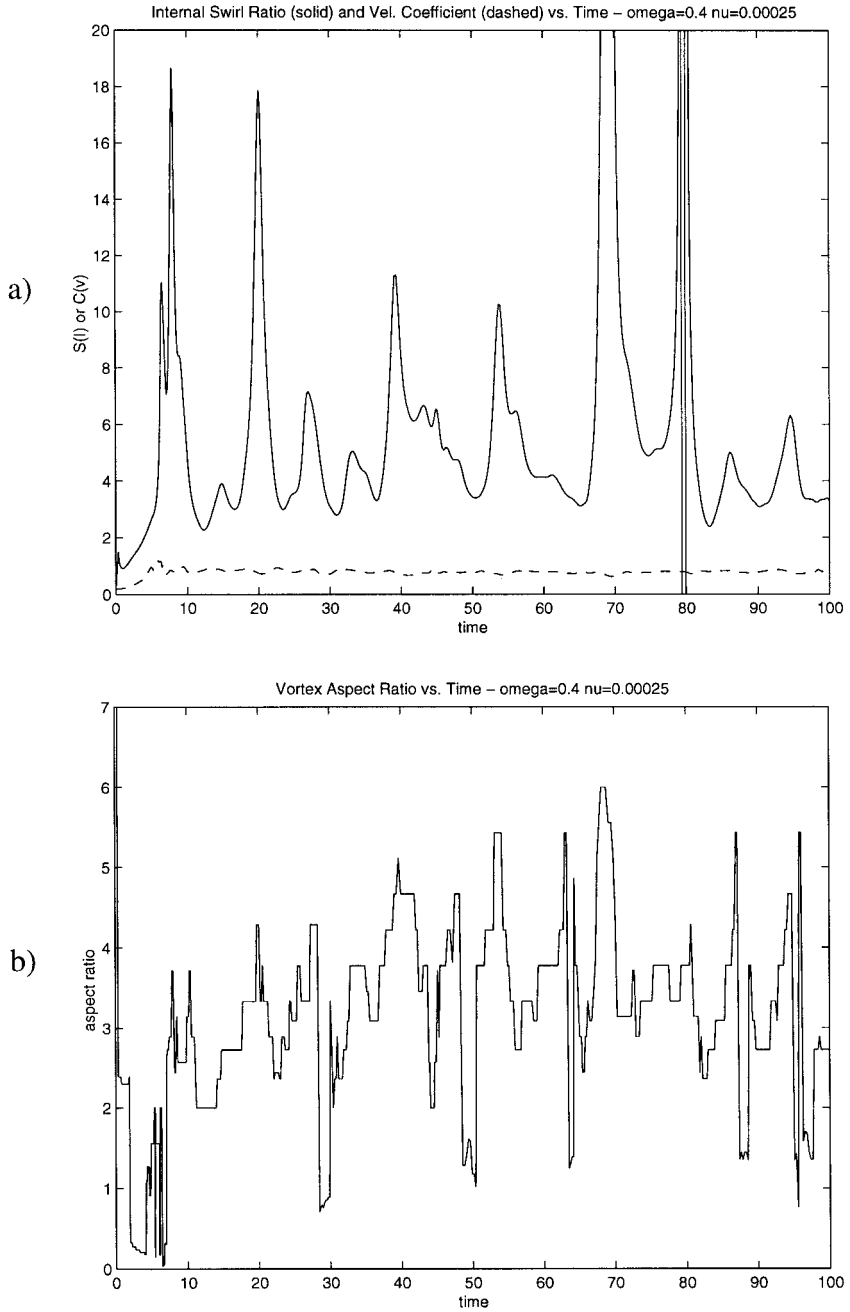

FIG. 9. (a) Internal swirl ratio S_I (solid line) and velocity coefficient C_v (dashed lined) during the simulation with $\Omega = 0.4$ and $\nu = 0.00025$; (b) vortex aspect ratio A_V for the same simulation.

and weaknesses of S_I versus A_V as indicators of the vortex flow structure. While S_I is always smoothly varying in time, it can become undefined and/or negative in highly unsteady flows when the flow direction temporarily reverses within the control volume, as it does in this case around $t = 80$. On the other hand, A_V takes on only discrete values and has discontinuous behavior in time but is well defined for all flow regimes and does not vary quite as wildly as S_I in the high swirl regime.

4. Dimensional analysis

Let us restrict ourselves to the case where there is only one fundamental length scale L in the model problem by assuming that the domain length scale and the height and width of the forcing field F_z are all roughly the same, as is the case for our model. (The radius of the domain has been chosen to be large enough so that it does not affect the dynamics; therefore, it does not

enter into the analysis.) We then have four dimensional parameters: the length scale L, the forcing scale F, the rotation rate Ω, and the viscosity ν. We may replace the forcing scale F with a convective velocity scale $U = w_{\mathrm{CAPE}}$ from (3.5). The equations of motion only relate velocities, so there are only two fundamental physical dimensions: length and time. Application of dimensional analysis (the Buckingham pi theorem) requires that the system must depend on only two dimensionless parameters. It is important to note that these two parameters are not unique. There are in fact four possibilities, from which we must choose two:

$$\mathrm{Re}_C = \frac{UL}{\nu}, \tag{4.1}$$

$$S_d = \frac{\Omega L}{U}, \tag{4.2}$$

$$\mathrm{Re}_V = \frac{\Omega L^2}{\nu}, \tag{4.3}$$

$$\Pi_4 = \frac{U^2}{\Omega \nu}, \tag{4.4}$$

where we have labeled each of the dimensionless groupings according to the following definitions: Re_C is the *convective Reynolds number*, a Reynolds number based on velocity scale of the convective forcing; S_d is a swirl ratio that we have labeled with the subscript d to indicate that it comes from dimensional analysis and to differentiate it from the laboratory swirl ratio (1.1); Re_V is the ratio of the far-field circulation to the viscosity, often called the *vortex Reynolds number* and is known to control the flow in laminar swirling boundary layers (see, e.g., Barcilon 1967); the physical significance of the last parameter is not known, though it can be written as Re_C/S_d.

Note that any two of these parameters together should contain all the information necessary to determine the outcome of the model; that is, we expect that ''observables'' such as S_I or C_v will be functions of the two dimensionless parameters we choose (albeit different functions for different choices of parameters). An obvious choice for one of the two dimensionless parameters to use for our study is the convective Reynolds number Re_C. Since $v_{\max} \sim U$ this is an appropriate Reynolds number for the problem. A natural choice for the other parameter is the swirl ratio S_d since this has the obvious connection to the swirl ratio used in laboratory models. However, we shall see in the following sections that the vortex Reynolds number Re_V is in fact more useful for predicting the characteristics of the flow in tornado-like vortices.

5. Exploration of parameter space

We now turn to the major area of investigation of this report: how do the structure and intensity of the vortex depend on the dimensionless parameters? To determine these relationships, we performed many numerical simulations of the type shown above, with different values for either Ω, ν, or the convective velocity scale U. Due to limits of computation time, these simulations were performed at a lower resolution of 64×64 grid points. Sets of simulations were performed with one of the parameters varying among the separate simulations and the other two held fixed. The simulations in all cases were integrated from $t = 0$ to $t = 200$, while the maximum velocities, S_I, RMW, and ZMW were recorded every 10 time steps during these simulations. The mean values and the variances of the data in each case were evaluated using the last 100 time units of the simulations.

Let us examine how the vortex changes as we vary S_d. Figure 10 shows the mean maximum velocities as the domain rotation rate Ω (equal to S_d since $U = L = 1$ in our nondimensional model) varies from 0.02 to 0.4. The model eddy viscosity is held fixed at $\nu = 0.001$ and the convective forcing is the F93 forcing (3.1). For very low rotation rates the radial and azimuthal velocities are very low, while the vertical velocities are relatively high. For higher rotation rates all three velocities increase, with the vertical velocities still exceeding the azimuthal velocities by about 50%. However, for larger rotation rates the vertical velocities decrease until they are substantially less than the azimuthal velocities. Over this range of higher values for Ω the maximum azimuthal and radial velocities decrease only slightly. Figure 11a shows the mean values of S_I, C_v, and A_V versus the rotation rate. Not surprisingly, S_I increases steadily with increasing Ω and A_V also increases, since RMW increases while ZMW decreases with increasing Ω. The velocity coefficient C_v has low values for the lowest values of Ω, due to the fact that an intense vortex does not form for very low values of the swirl ratio (see Fig. 1). However, for values of Ω where a vortex does form, C_v increases to a maximum of 0.88 when $\Omega = 0.08$ and decreases to 0.70 when $\Omega = 0.4$. This indicates that the efficiency with which the convective forcing is converted into azimuthal wind velocity decreases for large rotation rates.

How does the flow through the vortex core differ between the low rotation-rate and high rotation-rate regimes? Figure 12 shows close-ups of the velocity fields in the vortex core for the case when $\Omega = 0.1$ (Figs. 12a,b) and also when $\Omega = 0.4$ (Figs. 12c,d). In the first case the boundary layer inflow penetrates all the way to the $r = 0$ axis, then turns upward into a strong axial jet along the axis. It separates from the axis around $z = 0.4$. The maximum azimuthal velocity is $V = 0.83$, which occurs at $r = 0.1$ and $z = 0.23$. In the second case, the boundary layer inflow also penetrates to $r = 0$ and turns upward, but the vertical flow breaks away from the vertical axis at $z = 0.15$. The maximum azimuthal velocity is $V = 0.72$, occurring at $r = 0.12$ and at the much lower altitude of $z = 0.08$. Comparison of

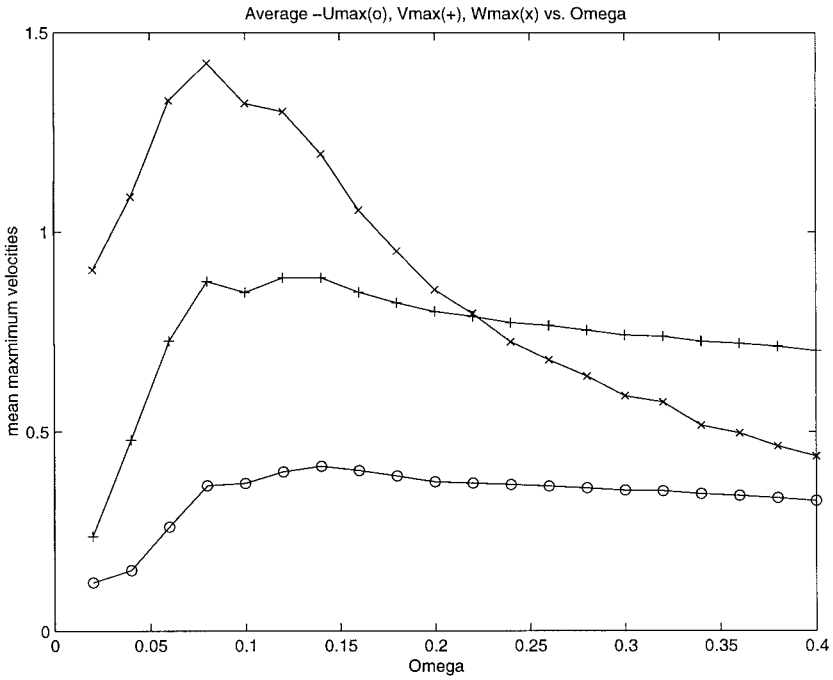

FIG. 10. Average maximum velocities as a function of the rotation rate Ω: radial velocities are marked by circles, azimuthal velocities are marked by $+$'s, and vertical velocities are marked by $\times$'s.

these two results with the illustrations of the structure of laboratory vortices as a function of swirl ratio indicates that the results with $\Omega = 0.1$ clearly reproduce a low-swirl intense vortex as shown in Fig. 1b, while the results with $\Omega = 0.4$ clearly reproduce a drowned vortex jump as shown in Fig. 1c. (Recall from section 3c that increasing Ω to 0.4 *and* decreasing ν to 0.00025 resulted in a vortex that occasionally was two celled in structure; the effect of ν on the vortex structure will be addressed shortly.) The steady increases of S_I and A_V as the vortex evolves between these states show how they are good indicators of the vortex structure.

The variance of S_I is a good indicator of the unsteadiness of the structure of the flow in the vortex core. Figure 11b shows the variance of S_I versus the rotation rate Ω. We can see that for values of Ω greater than 0.25 the variance increases suddenly from negligible values to values on the order of 0.5. The high variance of S_I when its average value is 2.5 or greater indicates that the flow in the vortex core is unsteady in this regime. Figure 13 shows a sample of the time evolution of the maximum velocities in the high-swirl regime shown in Figs. 12c,d. All three velocity maxima undergo steady oscillations, with the vertical velocities varying the most, as much as 20%. The period of oscillation is about six nondimensional time units, and the maxima in the vertical velocities lead the maxima in the radial and azimuthal velocities by about one time unit.

So far we have shown that as we increase S_d the vortex evolves in a manner similar to laboratory vortices when their swirl ratio S is increased, and that S_I and A_V are useful indicators of the structure and behavior of the flow. In laboratory experiments it has generally been found that the Reynolds number of the flow had a decreasing influence on the flow structure as it was increased (Church et al. 1979). If this is the case for our model, then we would expect that varying ν would not significantly affect on the flow structure—that it depends strongly on $S_d = \Omega L/U$. Thus we repeat the analysis varying the model eddy viscosity ν (equal to $1/\mathrm{Re}_C$ since $U = L = 1$) while now keeping the rotation rate $\Omega = 0.2$. Figure 14 shows the average maximum velocities for values of the ν varying from $\nu = 0.0004$ to $\nu = 0.0022$. The result is interesting in that the maximum velocities change with increasing ν in a manner that is opposite to how they changed with increasing rotation rate. By comparing Figs. 15a,b to Figs. 11a,b, we can make essentially the same observation with regard to the internal swirl ratio S_I, the velocity coefficient C_v, and the vortex aspect ratio A_V. We thus have the interesting observation that increasing the eddy viscosity has the same effect on the structure of the vortex as decreasing the domain rotation rate, and vice versa. Examination of the flows through the vortex core in the high and low eddy viscosity cases (not shown) gave nearly identical results to the low and high domain rotation rate results (respectively) shown in Fig. 12, confirming this observation. For the ranges of these parameters where an intense vortex is present, C_v changes relatively little. Furthermore, we see that in both cases

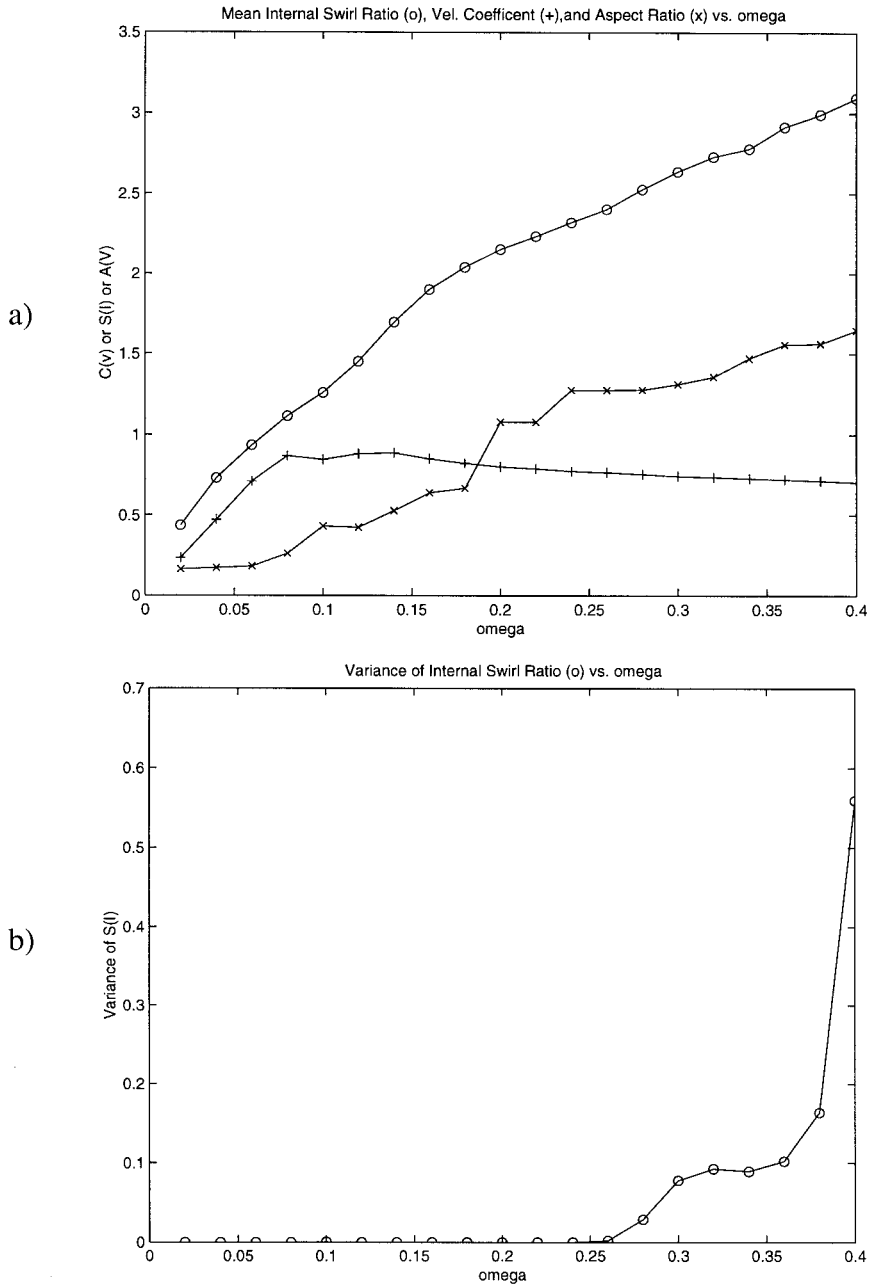

FIG. 11. (a) Average values for the internal swirl ratio S_I and the velocity coefficient C_v as a function of the rotation rate Ω of the domain. Here S_I is marked by the circles and C_V is marked by the +'s. (b) Variance of S_I as a function of the rotation rate Ω of the domain.

the onset of unsteady flow in the vortex core (as measured by the variance of S_I) occurs when S_I reaches a value of approximately 2.3.

This apparent reciprocal relationship between the rotation rate and the viscosity indicates that Re_V may be much more useful for predicting the structure of the flow in the vortex than the swirl ratio S_d. The matter remains unclear, however, since while varying ν changes Re_V and leaves S_d fixed, it also changes Re_C. To see how the flow evolves as we vary Re_C, while keeping Re_V fixed, we vary the convective velocity scale U while holding Ω and ν fixed. The results are shown in Fig. 16, where U increases from 0.316 to 1.414 while $\Omega = 0.4$ and $\nu = 0.001$; over this range Re_C increases from 316 to 1414. While S_I decreases by 20% as Re_C goes from 316 to 1000, it then appears to asymptote to a value of 2.2 for larger Re_C. Furthermore, this change in S_I only represents a small change in the actual struc-

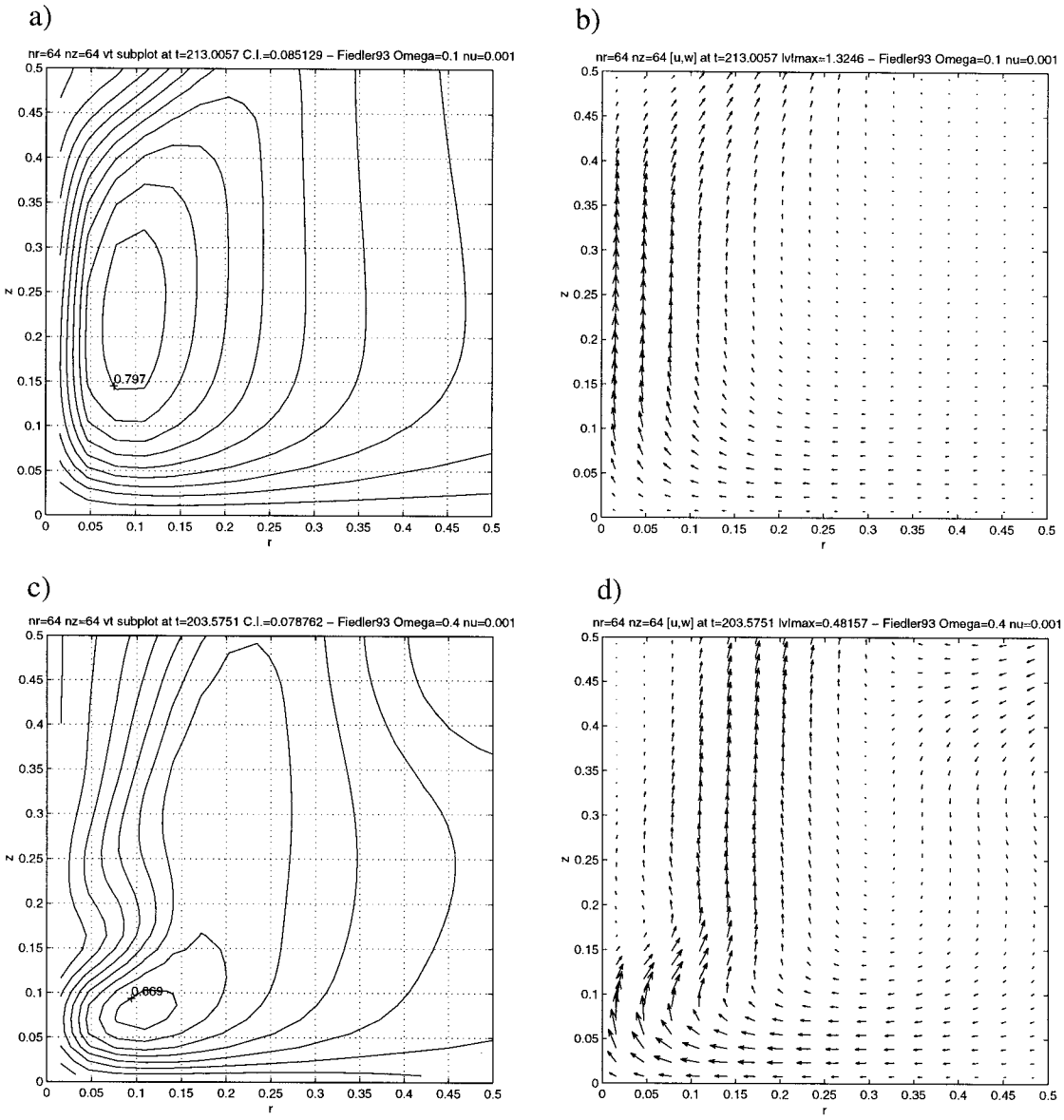

FIG. 12. Close-up of the velocity fields in the vortex core for two different domain rotation rates: (a) close-up of the azimuthal velocity field for $\Omega = 0.1$; (b) close-up of the meridional velocity vectors for $\Omega = 0.1$; (c) close-up of the azimuthal velocity field for $\Omega = 0.4$; and (d) close-up of the meridional velocity vectors for $\Omega = 0.4$. The contour intervals or maximum velocities are indicated at the top of each frame.

ture of the flow. Thus we observe only a weak dependence of the vortex structure on the convective Reynolds number.

6. Analysis

We have seen how, under simple convective forcing that causes convergence, a region of fluid in solid-body rotation collapses into an intense vortex near the surface. The highest azimuthal velocities occur during the development of the vortex, which then settles into a quasi-steady state with maximum velocities determined primarily by the strength of the convective forcing. There are two issues that call for further investigation: 1) what is the source of the oscillations observed in the maximum velocities for certain ranges of the parameters and 2) can we clarify and understand how the flow structure and behavior depend on the dimensionless parameters? We will address the former issue first.

a. Examination of the oscillations in the vortex core

In section 5 we saw that when Re_V is above a certain value, the flow through the vortex core is unsteady.

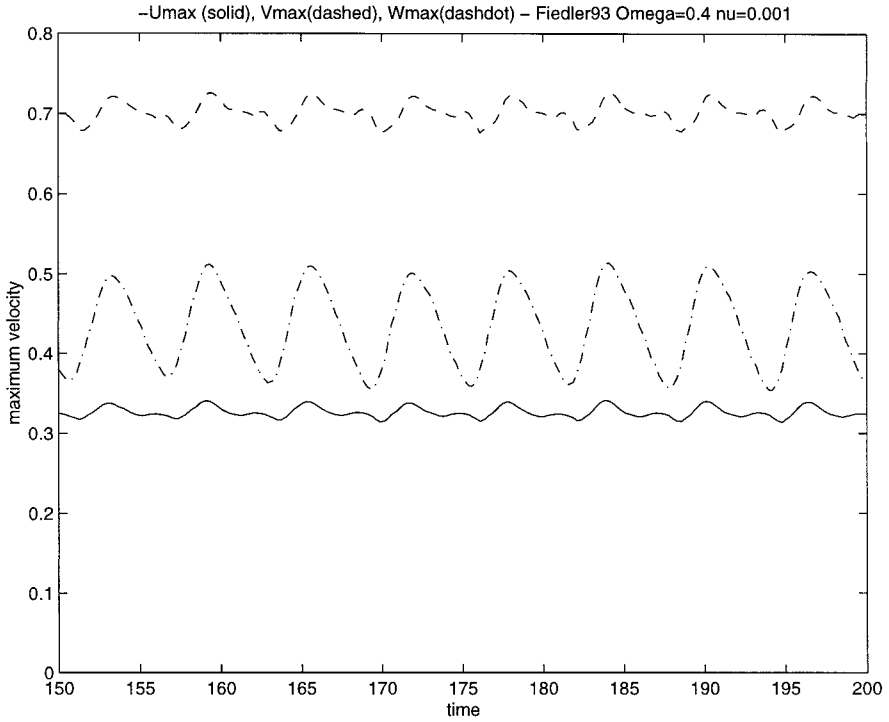

FIG. 13. A sample of the time evolution of the maximum velocities in an F93-type simulation with $\Omega = 0.4$ and $\nu = 0.001$: maximum inward radial velocities (solid), azimuthal velocities (dashed), and vertical velocities (dash–dot).

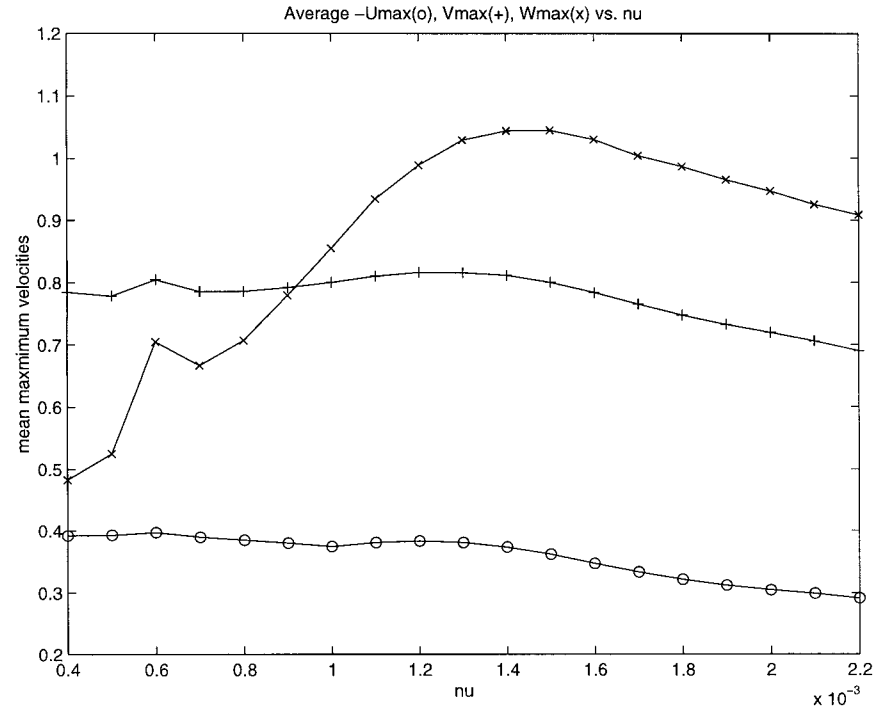

FIG. 14. Average maximum velocities as a function of the model eddy viscosity: average maximum radial velocities are marked by circles, azimuthal velocities are marked by +'s, and vertical velocities are marked by ×'s.

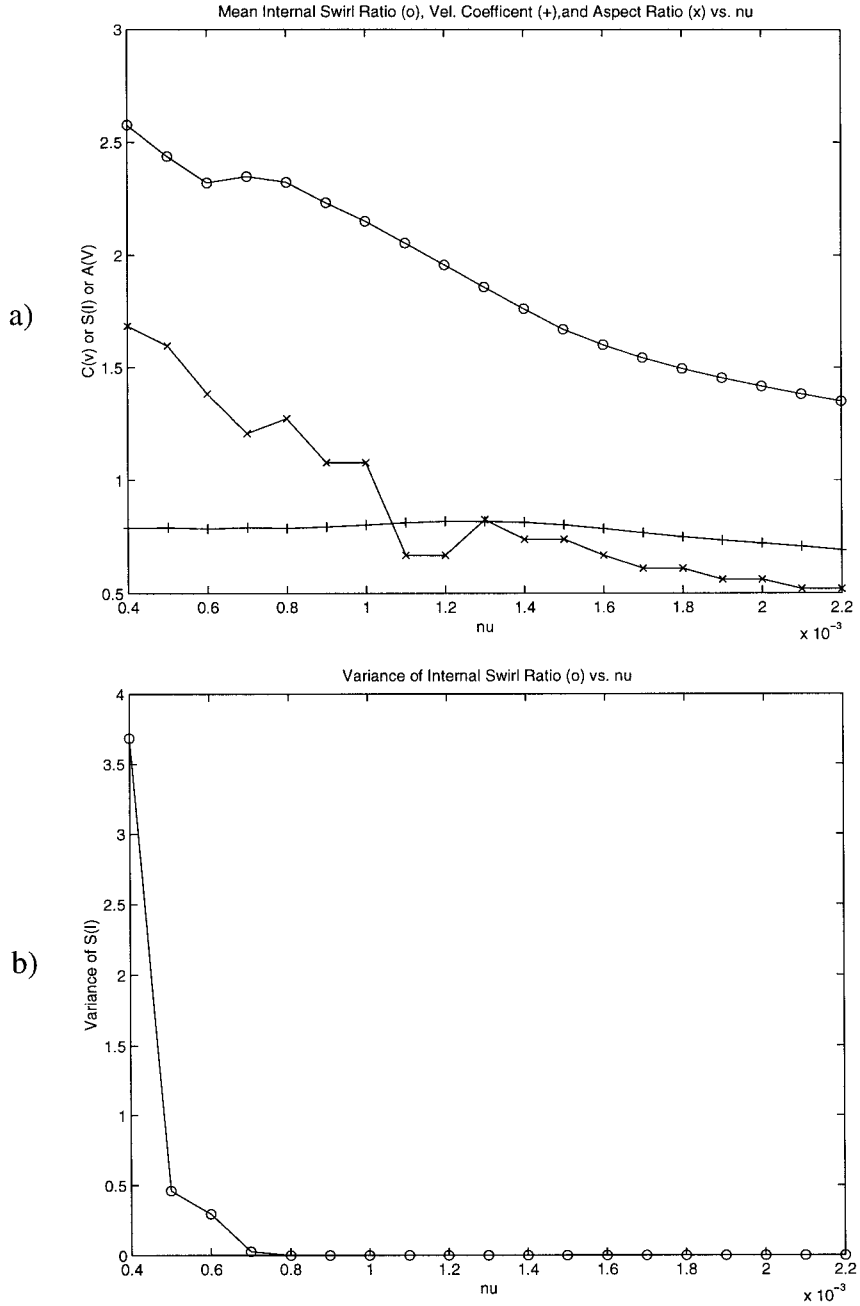

FIG. 15. (a) Average values for the internal swirl ratio S_I and the velocity coefficient C_v as a function of the model eddy viscosity ν. Here S_I is marked by the circles and C_v is marked by the +'s. (b) Variance of S_I as a function of the model eddy viscosity ν.

Figure 13 showed that this unsteadiness is associated with periodic (in some cases) oscillations in the values of the maximum velocities. What is the cause of these oscillations? Why are they not present in the low-swirl case?

To address these questions we first examined closely the velocity fields in the vortex core in the oscillatory regime. To achieve this, we ran a 64×64 gridpoint simulation, with $\Omega = 0.4$ and $\nu = 0.001$, from $t = 0$ to $t = 213$. We recorded the full velocity fields at 0.5 time unit intervals for the last 13 time units of the simulation. We then averaged the 26 fields to obtain an ''average'' state of the vortex during the oscillations. This allowed us to then derive deviations from this average state. Upon examination of these perturbation velocity fields, we observe axisymmetric disturbances propagating from the upper part of the domain down into the vortex core. These disturbances are shown in

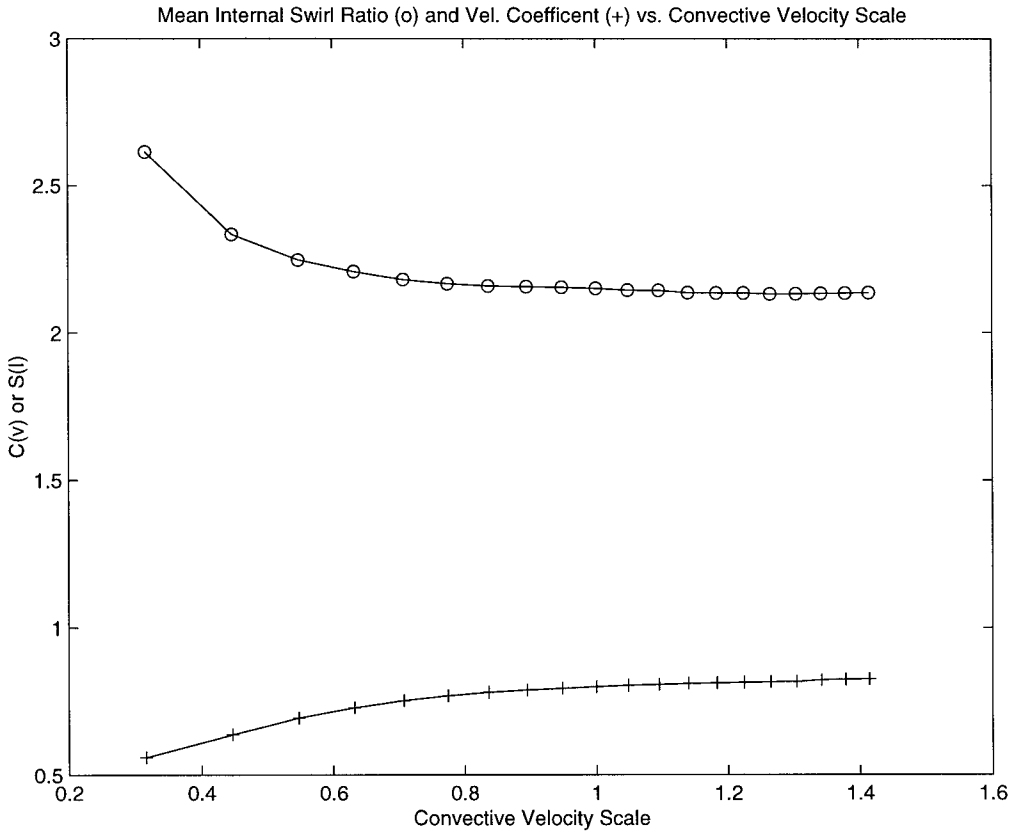

FIG. 16. Average values for the internal swirl ratio S_I and the velocity coefficient C_v as a function of the strength of the convective forcing; S_I is marked by the circles and C_v is marked by the +'s.

Figs. 17 and 18 in terms of the perturbation meridional vector velocity fields. In Fig. 17a, we can identify a clockwise circulation centered in the vicinity of $r = 0.1$, $z = 0.25$. In Fig. 17b, 0.5 time units later, this circulation can be seen to have moved downward slightly and is more distinct. This trend continues in the next two frames, and in Fig. 17d at $t = 202$ we can also see the beginnings of a reverse (counterclockwise) circulation appearing above $z = 0.3$. In the next series of plots (Figs. 18a–d) we can see this new circulation develops and descends until it is in approximately the same location as the original disturbance. Thus the cycle repeats itself indefinitely.

We repeated this analysis but instead for a flow with a steady vortex core by using the same parameters as before except with $\Omega = 0.15$, which puts the vortex in the low-swirl regime, without oscillations in the vortex core. Repeating the analysis above, we show in Fig. 19 a series of deviations of the meridional vector velocities from the mean. In this case, we see that the perturbations are orders of magnitude weaker than those we saw before, and rather than descending toward $z = 0.15$ where the maximum wind speeds occur, they are stationary. In fact, the plots show how the disturbances reversing in direction over time, like stationary waves.

Whether or not these waves propagate downward into the location of the maximum wind speeds is determined by the group velocities of the waves relative to the vertical velocity of the flow out of the vortex. When the vertical velocities are high enough to prevent these waves from penetrating to the surface, the vortex is said to be "supercritical," much like the flow upstream of a hydraulic jump. When the waves do penetrate to the surface, the vortex is considered to be "subcritical." From these definitions, we would say that the vortex is supercritical in the low-swirl case and subcritical in the high-swirl case.

b. Eigenanalysis of axisymmetric disturbances in the vortex core

The first place to look for a basic understanding of such disturbances is in the analysis of linearized disturbances on the mean flow. However, the question at hand is not simply one of the existence of unstable modes. The likely source for the disturbances is the region of highly unsteady flow where the vortex outflow sheds vortices and becomes two-dimensional (axisymmetric) turbulence (see Fig. 8b, for example). Therefore, the flow in the vortex core does not need to be unstable but rather needs to support downward-propagating

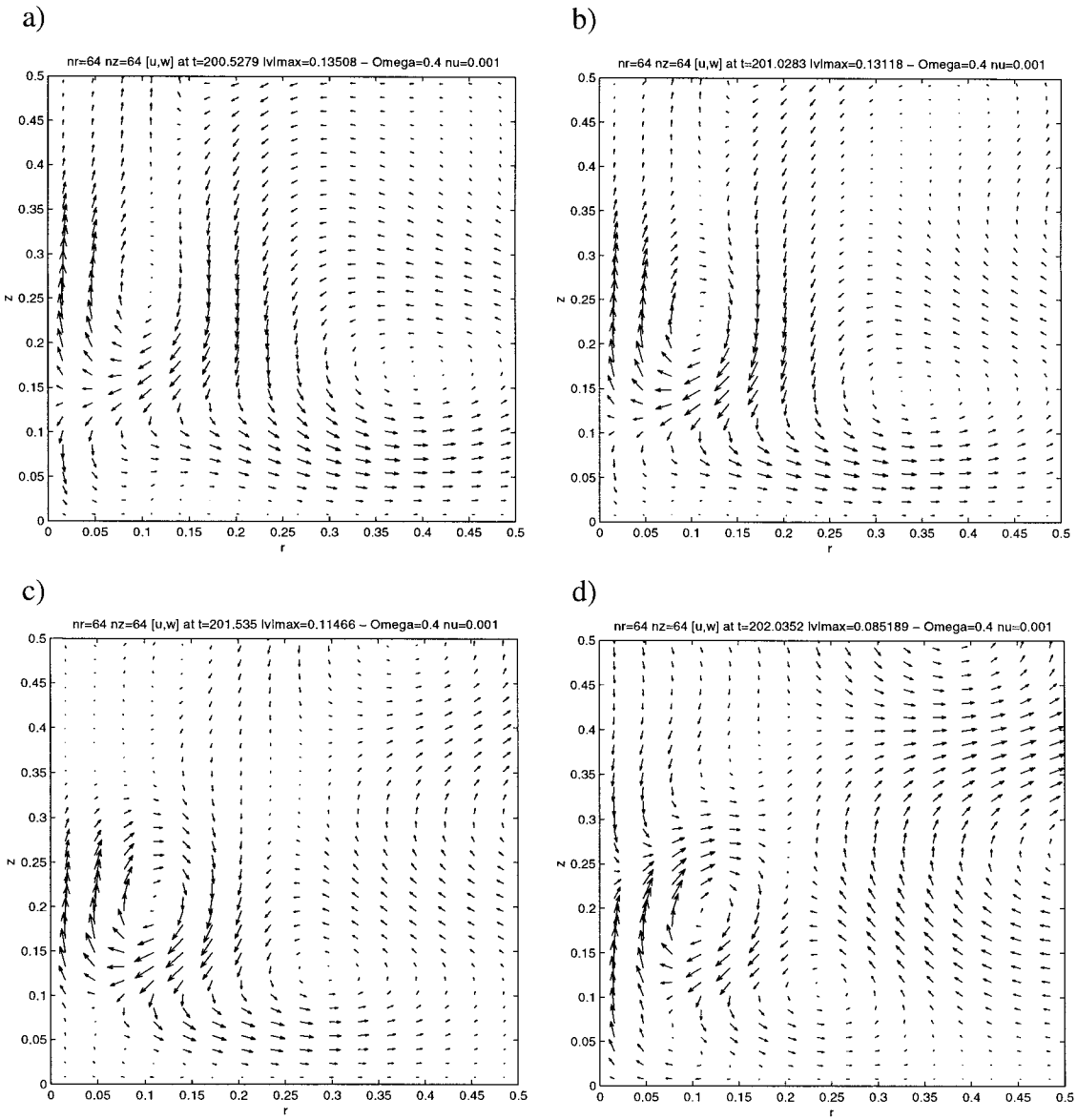

FIG. 17. Meridional vector velocity plots of the deviations from the average velocity field of the vortex in the oscillatory, high-swirl regime: deviation from the mean at (a) $t = 200.5$, (b) $t = 201.0$, (c) $t = 201.5$, and (d) $t = 202.0$. The plots show the domain from $0 < r < 0.5$, $0 < z < 0.5$. The maximum velocity deviations are indicated at the top of each frame.

waves that reach the surface. Linear instability is, of course, also a possible cause for the disturbances.

The dynamics of axisymmetric (inertial) disturbances in axisymmetric swirling flows have received considerable attention in the field of hydrodynamic stability. Early work on the stability of swirling flows to axisymmetric disturbances were those of Rayleigh (1880), for inviscid flows, and Taylor (1923), for viscous flows, which are summarized in the subsequent texts such as Lamb (1932), Chandresekhar (1961), and Drazin and Reid (1981). In our case we are particularly interested in the dynamics of axisymmetric disturbances in a viscous axisymmetric flow with shear in the azimuthal and vertical winds. We neglect the radial wind since it is clearly much smaller than the other velocity components in the region of interest. We would like to show that the disturbances we observe above are indeed associated with the shear of the vertical and azimuthal winds.

Equations for the structure and phase speed of axisymmetric disturbances in a viscous flow with shear in both the vertical and azimuthal winds are derived in section 79 of Chandresekhar (1961) for swirling flows with azimuthal velocities of the form $V(r) = Ar + B/r$ (where A and B are constants; this is the general solution for a steady viscous swirling flow between rotating cyl-

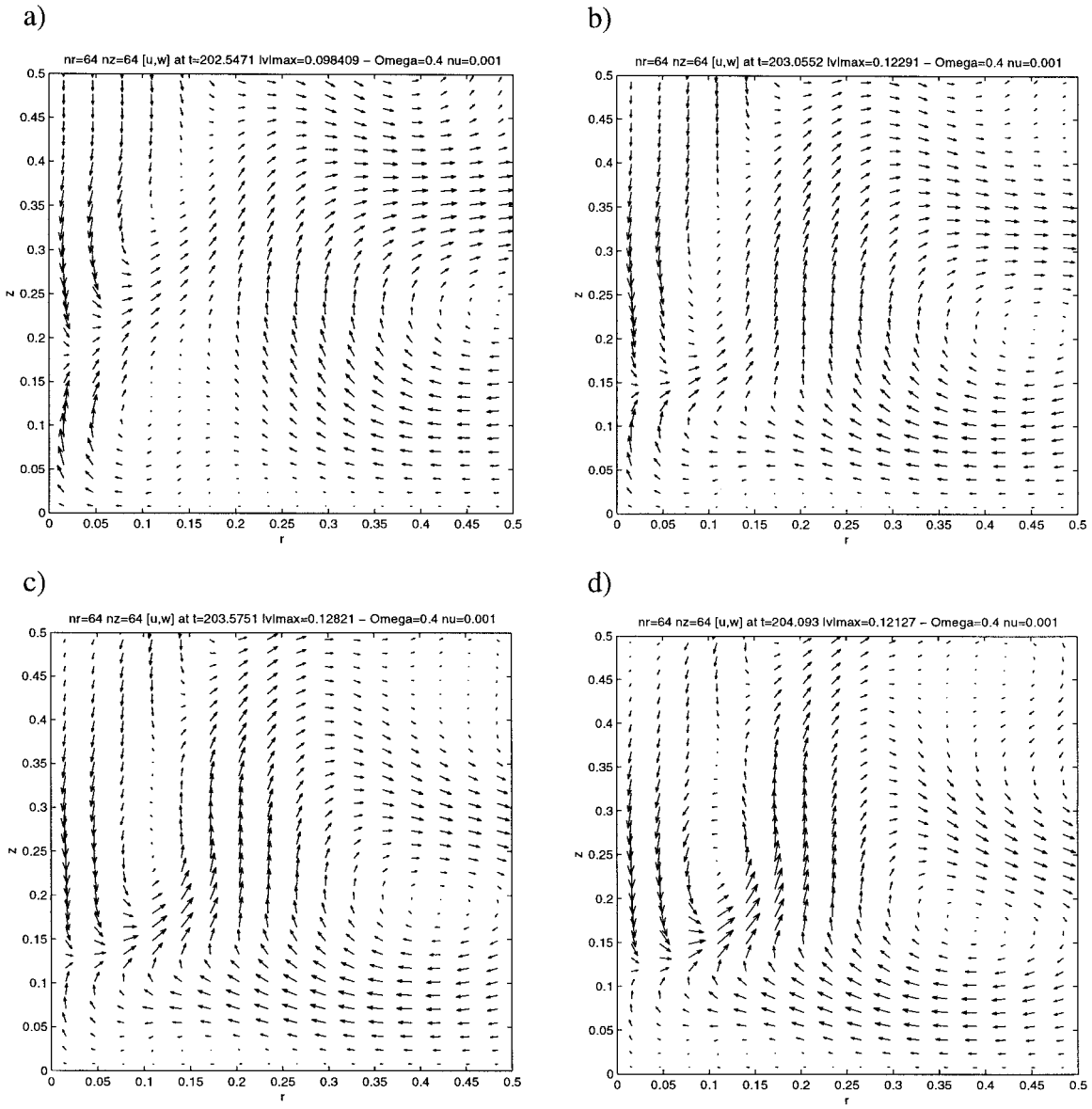

FIG. 18. Meridional vector velocity plots of the deviations from the average velocity field of the vortex in the oscillatory, high-swirl regime: deviation from the mean at (a) $t = 202.5$, (b) $t = 203.1$, (c) $t = 203.6$, and (d) $t = 204.1$. The plots show the domain from $0 < r < 0.5$, $0 < z < 0.5$. The maximum velocity deviations are indicated at the top of each frame.

inders). These equations describe the evolution of small disturbances of the form

$$u'(r, z, t) = \hat{u}(r)e^{i(kz+\omega t)}, \tag{6.1}$$

and so on for the perturbation azimuthal and vertical velocities. Modifying those equations for arbitrary azimuthal velocity profiles, we have a system of two equations for the perturbation velocity functions $\hat{u}(r)$ and $\hat{v}(r)$, in a background flow with mean vertical velocity $W(r)$ and mean azimuthal velocity $V(r)$:

$$[\nu DD_* - \nu k^2 - i(\omega + kW)](DD_* - k^2)\hat{u} + ikr\hat{u}\left[DD_*\left(\frac{W}{r}\right)\right] = \frac{2Vk^2}{r}\hat{v} \tag{6.2}$$

$$[\nu DD_* - \nu k^2 - i(\omega + kW)]\hat{v} = \left(\frac{dV}{dr} + \frac{V}{r}\right)\hat{u}, \tag{6.3}$$

where $D = \partial/\partial r$, $D_* = \partial/\partial r + 1/r$, and the boundary conditions are

$$\hat{u} = DD_*\hat{u} = \hat{v} = 0 \quad \text{at } r = 0 \tag{6.4}$$

$$\hat{u} = D\hat{u} = \hat{v} = 0 \quad \text{at } r = R. \tag{6.5}$$

This eigenvalue problem for ω can be solved by discretizing the system such that the functions V, W, $\hat{u}$, and $\hat{v}$ are replaced by vectors of finite length, and the differential operators are replaced by matrix representations of their usual centered finite-difference approxi-

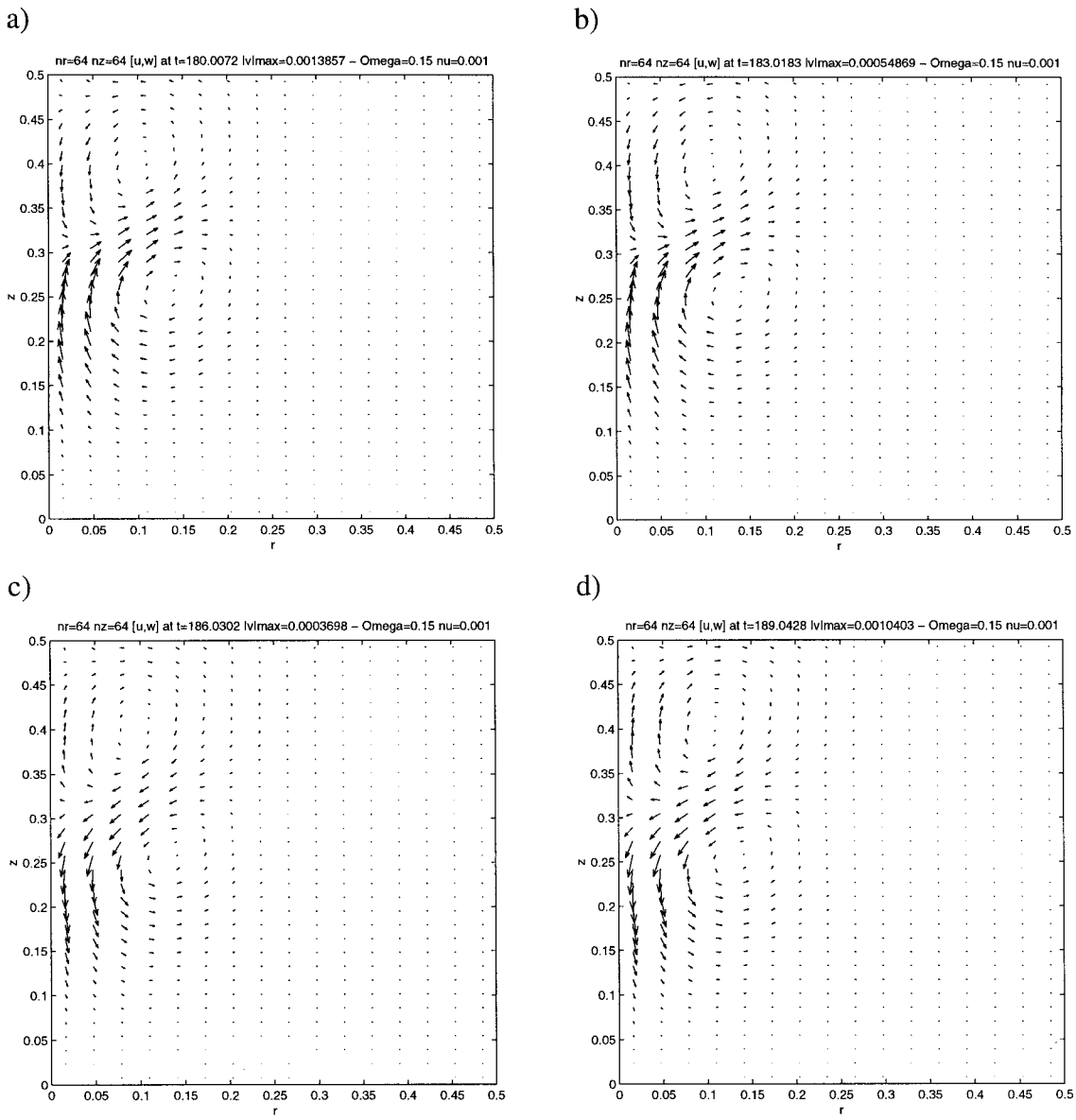

FIG. 19. Meridional vector velocity plots of the deviations from the average velocity field of the vortex in the steady, low-swirl regime: deviation from the mean at (a) $t = 180.0$, (b) $t = 183.0$, (c) $t = 186.0$, and (d) $t = 189.0$. The plots show the domain from $0 < r < 0.5$, $0 < z < 0.5$. The maximum velocity deviations are indicated at the top of each frame.

mations. By writing the perturbation vectors as a single state vector **x**,

$$\mathbf{x} = \begin{bmatrix} \mathbf{u} \\ \mathbf{v} \end{bmatrix}, \tag{6.6}$$

the system of equations (6.2)–(6.5) may be reduced to a single discrete eigenvalue problem,

$$\mathbf{A}\mathbf{x} = \omega\mathbf{B}\mathbf{x}, \tag{6.7}$$

which can be solved with standard generalized eigenvalue routines.

The mean flows $V(r)$ and $W(r)$ were acquired from radial profiles of the average azimuthal and vertical velocity fields described in section 6a, for both the high-swirl case with $\Omega = 0.4$ and the low-swirl case with $\Omega = 0.15$. We used the radial profiles of velocity at $z = 0.31$ since the axisymmetric disturbances appeared to be very robust at this height. These profiles are shown in Fig. 20. We first chose $k = 15.7$, which corresponds to a vertical wavelength of 0.4, our best estimate for the axisymmetric disturbances identified above. We set the viscosity to be the same as in the numerical simulation: $\nu = 0.001$.

We looked for modes similar in structure to the disturbances we observe, with negative phase speeds and

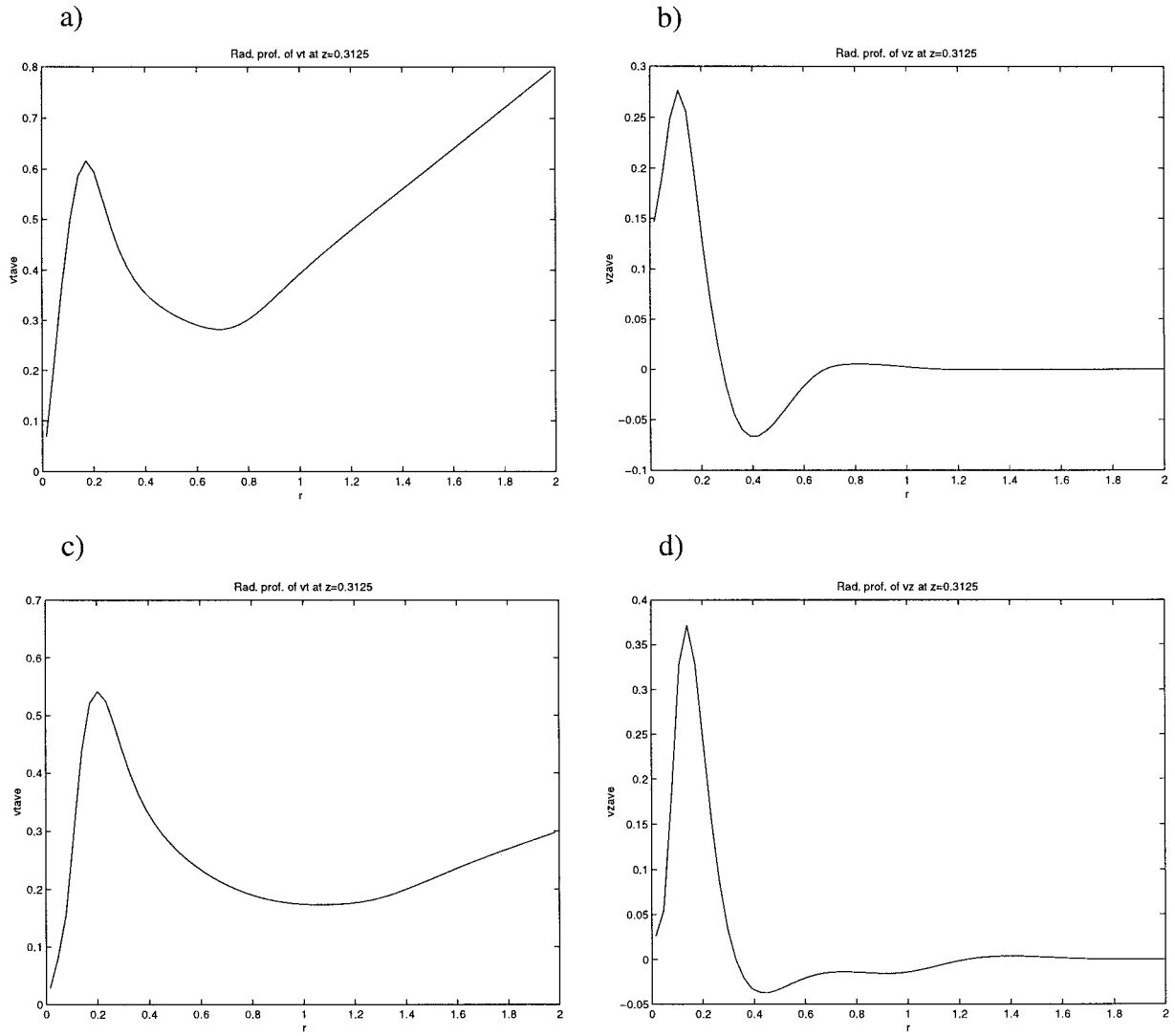

FIG. 20. Radial profiles of average azimuthal and vertical velocities at $z = 0.3125$ in the two simulations considered in section 6a: (a) azimuthal velocity, high-swirl case; (b) vertical velocity, high-swirl case; (c) azimuthal velocity, low-swirl case; and (d) vertical velocity, low-swirl case.

zero or negative group velocities. The dissipation rates for all the modes are surprisingly high, with the imaginary parts of their eigenvalues being on the order of 0.5. The structures with the lowest dissipation rates are not similar to the axisymmetric disturbances identified above but rather reside far away from the axis in the most quiescent part of the flow. However, we were able to identify modes that are similar to the disturbances we are looking for by selecting the one with the largest perturbation radial velocities $\hat{u}(r)$ in the vicinity of $r = 0.1$. This mode is shown in Fig. 21 and compares well to the disturbance shown in Fig. 17b.

While we have not identified the source of these disturbances as spontaneously growing unstable modes in the vortex core, some useful information can be found by examination of the phase speeds and group velocities of these modes in the high- and low-swirl cases. Figure 22 shows plots of the phase speed $c_p = -\omega/k$, decay rate $\mathrm{Im}\{\omega\}$, and the real parts of the eigenvalues ω, as a function of k for the two examples. The group velocity $c_g = -d\omega/dk$ may be inferred from the plots of the $\mathrm{Re}\{\omega\}$. We see that in the high-swirl case, the modes with $k = 15.7$ have a phase speed of -0.18 and a group velocity of $+0.07$; by comparison, the disturbances we observed in the model had a phase speed of roughly -0.04. In the low-swirl case, the phase speed is -0.05 and the group velocity is $+0.15$. Therefore, the tendency for linear disturbances to travel down the vortex core and reach the surface is much less in the low-swirl case than in the high-swirl case. While modes with downward group velocities were present for all wavenumbers in both cases, such modes were not similar to the dis-

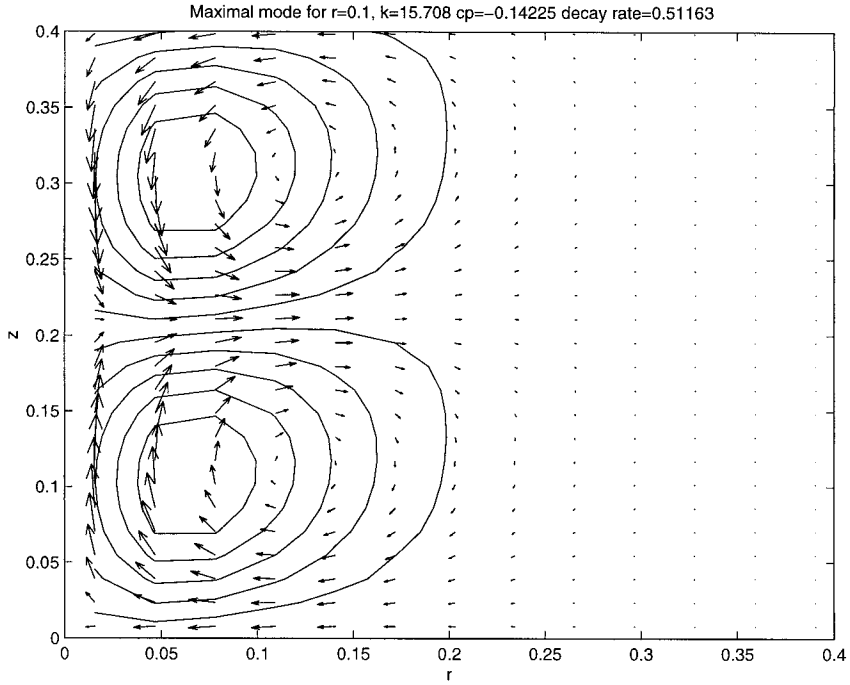

FIG. 21. Modal structure with vertical wavelength 0.4 and maximum radial velocities at $r = 0.1$ found from eigenanalysis of the vortex core in the high-swirl case.

turbances identified in the numerical simulations, but rather were associated with the downward recirculation outside of the vortex. Note also that Fig. 22b does indicate the existence of modes near the axis with zero or negative group velocities for wavenumbers $k < 12$ in the high-swirl case.

The large amplitudes of the downward-propagating disturbances shown in Figs. 17 and 18 (as much as 50% of the mean flow) suggest that their dynamics is very nonlinear. This nonlinearity may account for their persistence and their shorter wavelengths in comparison to the predictions of the linear theory. It is also quite likely that the rapid variation with height in the structure of the vortex is important, so that ultimately a successful analysis of the disturbances will require a full eigenanalysis of the flow in the entire domain.

c. *The results of further explorations of parameter space*

Measurement of the internal swirl ratio S_I offers a way to characterize the state of the vortex as the parameters are varied. We have seen that, for values of S_I above 2.5, the flow at the vortex core is highly oscillatory, with alternating periods of strong and weak meridional flow through the vortex core. The internal swirl ratio, and the behavior of the vortex, appears to depend very strongly on the vortex Reynolds number and only weakly on the convective Reynolds number, with this weak dependence decreasing for increasing convective Reynolds number.

To further explore the apparently reciprocal nature of the rotational forcing and the eddy viscosity, we performed a large number of 64×64 resolution simulations with varying values of both Ω and ν. Through the use of the Cray T3E at the National Energy Research Scientific Computing Center, we were able to efficiently produce an ensemble of 120 simulations with varying parameters. We found mean values and variances of the velocities, the internal swirl ratio, and the velocity coefficient for the parameter space defined by $\Omega = 0.06, 0.09, \ldots, 0.33$, and $\nu = 0.0006, 0.0007, \ldots, 0.0017$. The results are depicted in Figs. 23, 24, and 25, which show the mean internal swirl ratio, the variance of the internal swirl ratio, and the mean velocity coefficient, respectively, as functions of Ω and ν.

If the structure of the vortex did indeed depend solely on the vortex Reynolds number, then we would expect the internal swirl ratio (and vortex structure) to be purely a function of Re_V:

$$S_I = S_I(\mathrm{Re}_V) = S_I\left(\frac{\Omega L^2}{\nu}\right). \tag{6.8}$$

If this were the case, then S_I would have constant values on rays emanating from the origin of the Ω–ν plane. For the most part, this is indeed what Fig. 23 indicates. Figure 24 shows how the vortex makes the transition from steady to unsteady flow for $\mathrm{Re}_V > 270$, where the variance in S_I increases sharply. It also increases sharply again for $\mathrm{Re}_V > 400$; this appears to be associated with

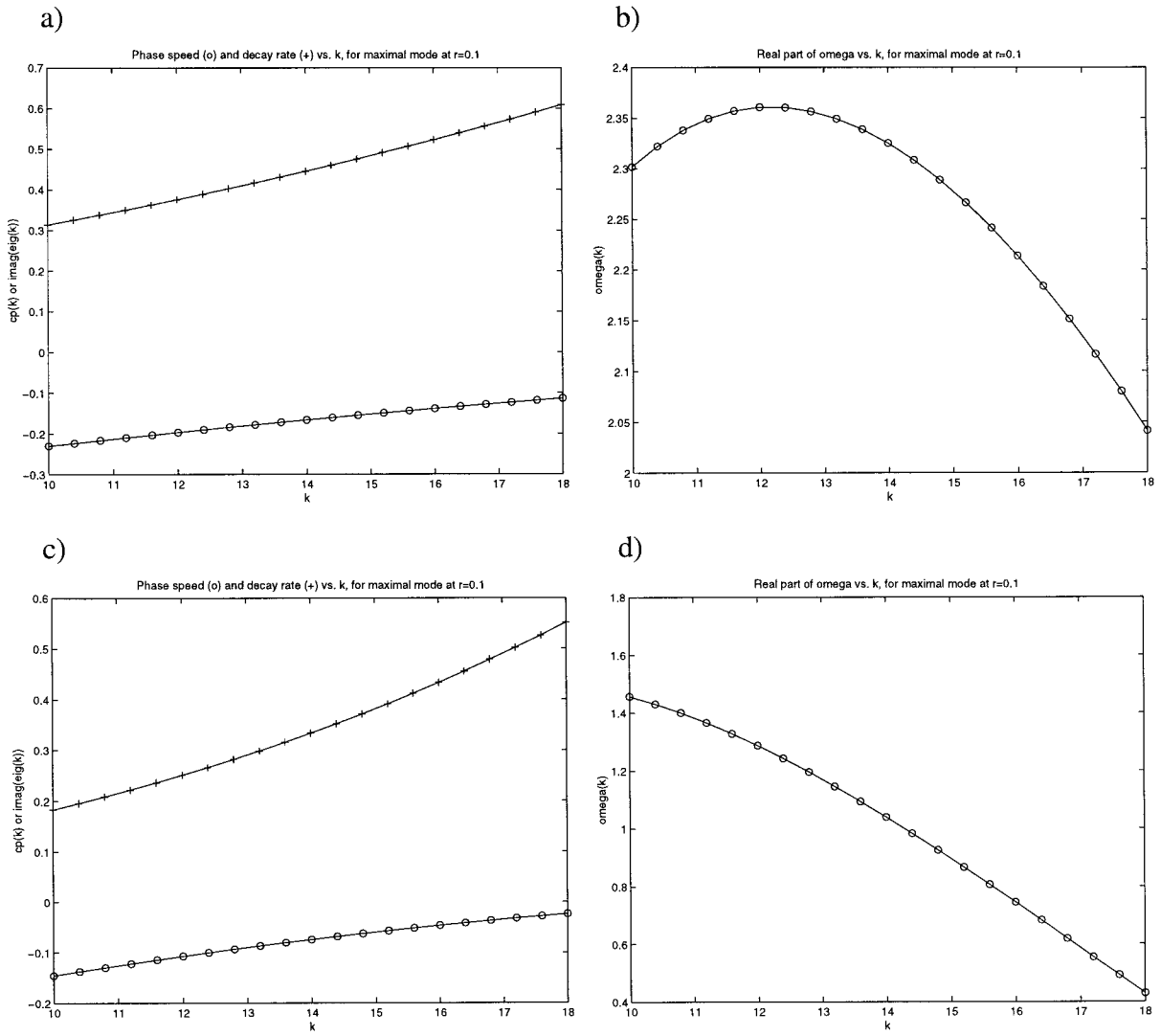

FIG. 22. Plots of phase speed, decay rate, and the real parts of ω vs vertical wavenumber k for the modes with maximum amplitude at $r = 0.1$: (a) phase speed and decay rate, high-swirl case; (b) ω, high-swirl case; (c) phase speed and decay rate, low-swirl case; and (d) ω, low-swirl case.

the episodic appearances of a two-celled vortex structure.

There are two caveats to the success of these results: 1) examination of the contours of S_I showed that they did not extrapolate exactly back to the origin, but rather to a point where $\nu = 0$ and Ω has a small positive value; and 2) the hypothesized dependency for S_I breaks down for large Ω and small ν. For the present we can only speculate as to the cause of these anomalies. Note that the deviations from (6.8) for large Ω and ν are also associated with unsteady flow in the vortex core, as shown in Fig. 24. A very likely cause of this discrepancy is that 100 time units may not be long enough to compute the correct mean, due to the extreme variability of S_I when the vortex Reynolds number is large, as is clearly shown in Fig. 9a. In fact, the vortex aspect ratio was much more consistent with a relationship such as (6.8) in this part of parameter space (not shown), probably due to its lesser variability in the unsteady regime as shown in Fig. 9b. It is also very likely the solutions are underresolved by the model for large Re_V. We can offer one hypothesis as to why the curves of constant S_I do not extrapolate exactly back to the origin. Grid-based numerical models of the Navier–Stokes equations generally have a small amount of built-in numerical viscosity, which effectively increase the actual viscosity of the model. If we take this additional viscosity into account, the lines of constant S_I may indeed trace back to the origin where the true viscosity is zero.

The results in Fig. 25 for the velocity coefficient C_v show a more complicated structure. The maximum azimuthal velocities increase both for decreasing Ω *and*

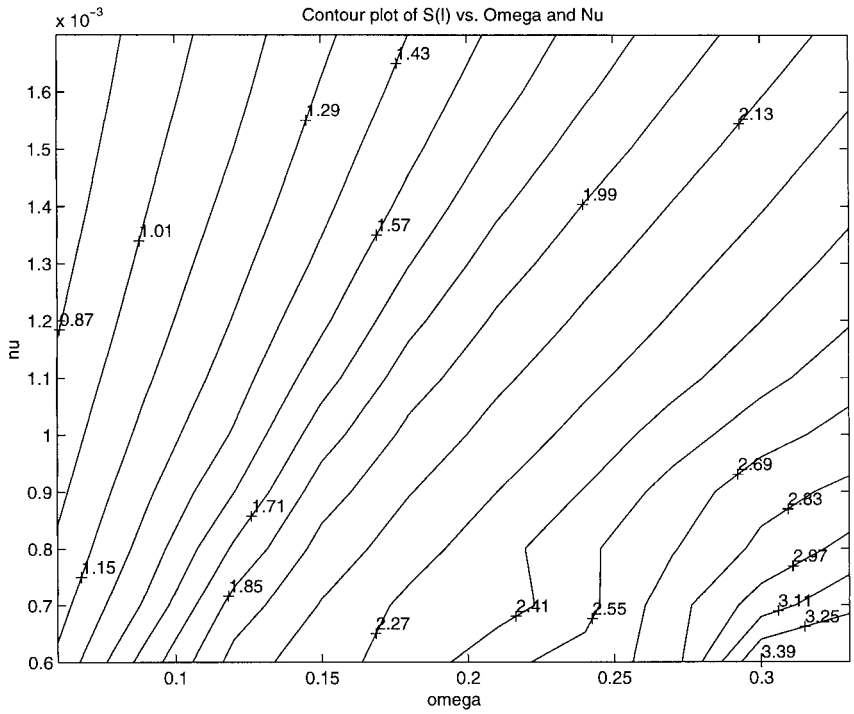

FIG. 23. Contour plot of the mean value of the internal swirl ratio as a function of the domain rotation rate Ω and the eddy viscosity ν.

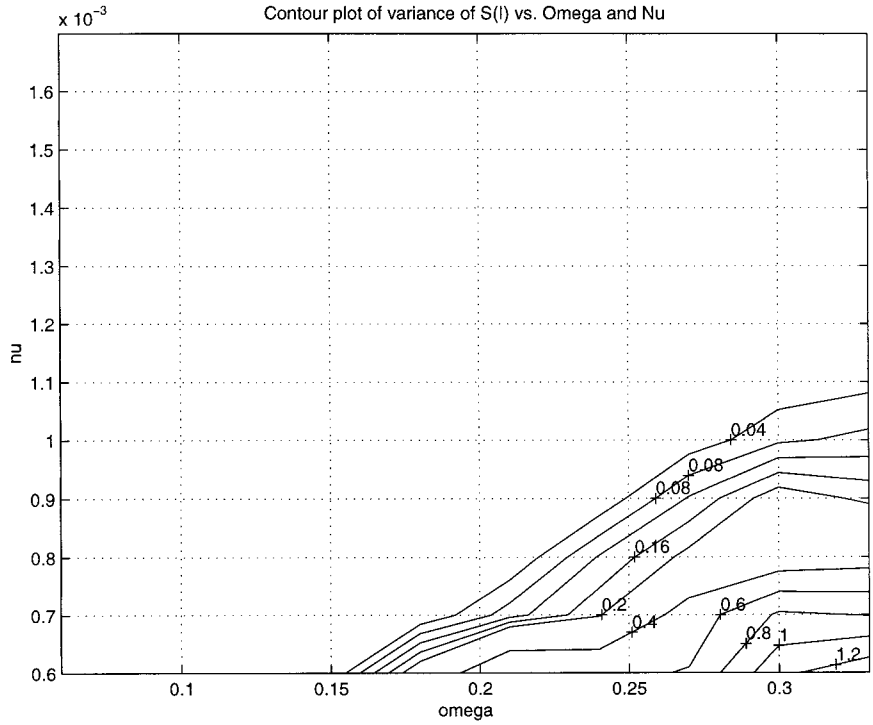

FIG. 24. Contour plot of the variance of the internal swirl ratio S_I as a function of the domain rotation rate Ω and the eddy viscosity ν. Due to the wide range in values for the variance, the contour levels have been chosen arbitrarily to have the following values: 0.04, 0.08, . . . , 0.16; 0.2, 0.4, . . . , 1.2.

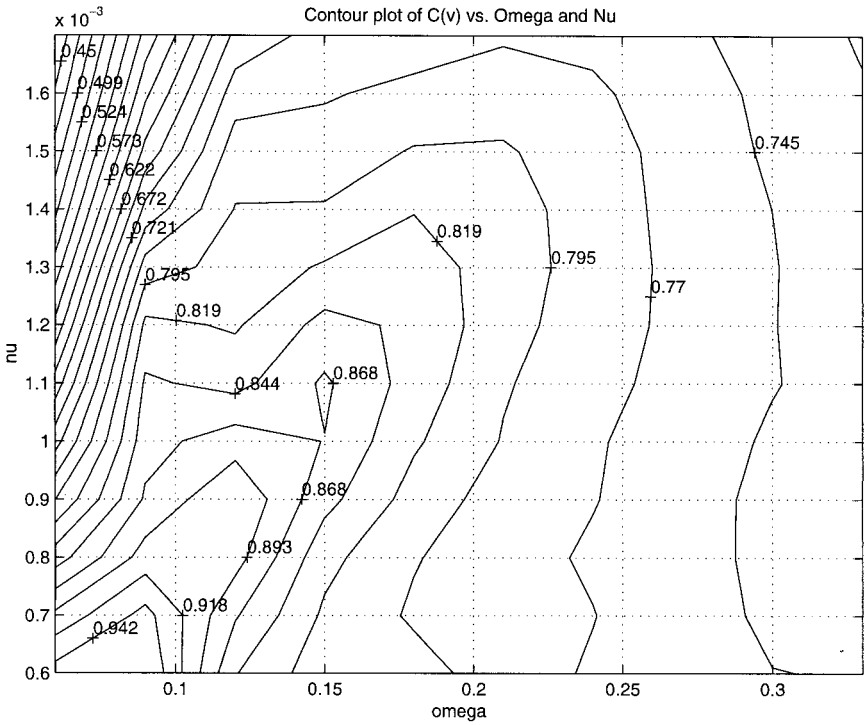

FIG. 25. Contour plot of the mean value of the velocity coefficient C_v as a function of the domain rotation rate Ω and the eddy viscosity ν.

decreasing ν, and for each value of ν there is a particular value of Ω that produces the highest azimuthal velocities. By finding the ray in the Ω–ν plane that is coincident with maximum C_v values, we find that the vortex Reynolds number that maximizes the wind speeds is $\mathrm{Re}_V = 140$. The fact that C_v increases with increasing Re_C and is maximized for $\mathrm{Re}_V = 140$ is clearly illustrated by the results in Fig. 26, which show C_v as a function of U and Ω (which are proportional to Re_C and Re_V, respectively). Here C_v increases with Re_C because of the decreasing losses of angular and radial momentum in the surface boundary layer.

Why does the structure and behavior of the flow depend so strongly on the vortex Reynolds number (and only weakly on Re_C)? The structure of the flow depends very strongly on the volume rate of the flow up through the axis of the vortex, which is ultimately determined by the strength of the radial inflow in the surface boundary layer and whether or not this radial inflow penetrates to the axis at $r = 0$. The surface boundary layer, in turn, can be approximated by the boundary layer beneath a potential vortex. From the ''point of view'' of the boundary layer, Γ and ν are the only dimensional parameters. The dynamics of swirling boundary layers and their strong dependence on Γ/ν has been previously discussed by Barcilon (1967), Burggraf et al. (1971), and Serrin (1972). Therefore, these parameters control the radial inflow, which in turn determines the structure and behavior of the vortex.

7. Conclusions

Our results are in general agreement with previous tornado vortex research, with the important new observation of the controlling effect of the vortex Reynolds number on the structure and maximum wind speeds of axisymmetric tornado-like vortices. This result is important for two reasons. First, it unifies the results of previous papers, such as those by Rotunno (1979), Walko and Gall (1986), Howells et al. (1988), and F94 and F95, which reported a variety of results regarding vortex structure and maximum wind speeds for a variety of values for the rotational forcing and eddy viscosity. For example, in regards to how the model parameters affected the maximum wind speeds, F94 reported that, ''The decrease in viscosity has little effect on the maximum windspeed of the most intense vortex, but has a large effect on the value of 2Ω that produces the most intense vortex. With $\nu_0 = 2.5 \times 10^{-4}$, the most intense vortex occurs with $2\Omega = 0.07$ . . . . With $\nu_0 = 1.25 \times 10^{-4}$, the most intense vortex occurs with $2\Omega = 0.04$ . . . .'' Thus Fiedler observed that the maximum wind speed as a function of the rotation rate was different for different viscosities; in fact, for this example the rotation rate of maximum wind speed is approximately halved when the viscosity is halved. This is indeed the relationship we have demonstrated and explained.

The second reason these findings are important is that they indicate how these vortices will behave as we in-

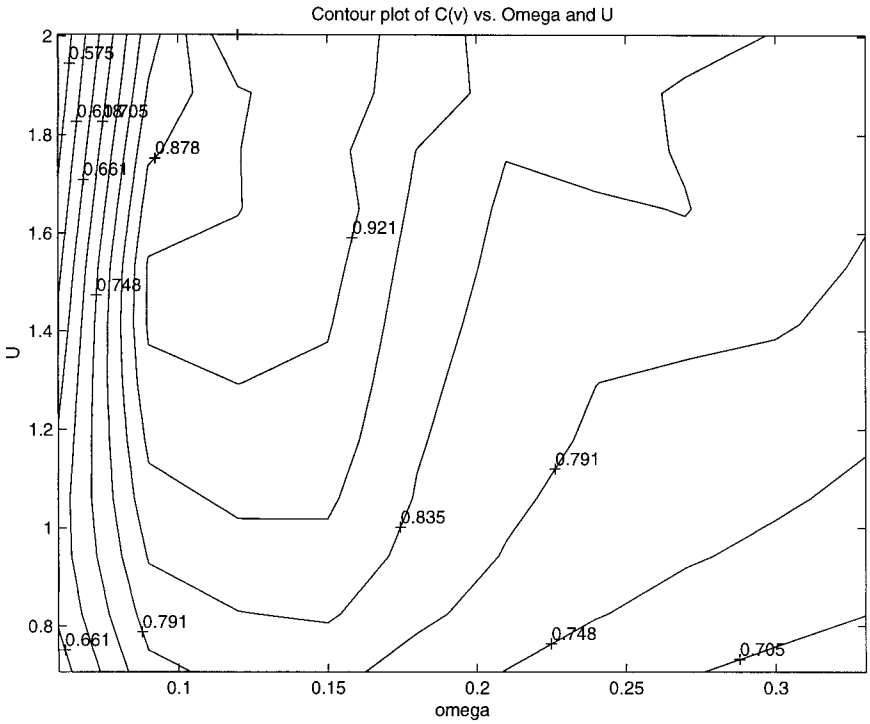

FIG. 26. Contours of the velocity coefficient C_v as a function of the convective velocity scale U and the rotation rate Ω.

crease the Reynolds number to values that apply to the atmosphere. In particular, we see two trends that are significant: 1) as the model eddy viscosity is decreased, the maximum possible wind speed (for the best choice of rotation rate) increases; and 2) less and less rotational forcing is required to achieve that maximum wind speed. This first point is significant because it means that axisymmetric models may yet produce realistic tornado wind speeds if they can be run with more ''realistic'' Reynolds numbers. The second point is particularly important because one of the obvious weaknesses of current numerical tornado-vortex simulations is that they supply the vortex with a steady, symmetric, and unlimited field of rotating fluid. Our results show that as the Reynolds number is increased, less and less rotation will be necessary to produce a realistic tornado vortex.

Our conclusions have some interesting implications for real tornadoes and the wide variety of structures and behaviors they exhibit. Tornado afficionados are familiar with two typical tornado structures: the tight, wound-up vortex with a nearly laminar appearance (typical of waterspouts, for example); and the broad, diffuse vortex with a wide base and an extremely turbulent flow (typical of severe tornadoes in the central United States). In analogy with the laboratory experiments, these two cases have been recognized as vortices in the low-swirl and high-swirl regimes, respectively. Our results suggest that the structure of a tornado is determined entirely by the angular momentum of the background rotating wind field and an as yet undetermined appropriate value for the turbulent eddy viscosity, which may depend on various factors such as surface roughness. Given these parameters, the maximum wind speeds will then be the proportional to the intensity of the convection that supplies the vertical forcing (the overhead thunderstorm) and to the appropriate value of the velocity coefficient C_v.

The structure and dynamics of actual tornadoes will therefore depend crucially on the details of their turbulent swirling boundary layers. This leads to the inevitable conclusion that a complete understanding of tornado vortices that can make more precise claims for observables such as the maximum wind speeds will require an understanding of how a fully turbulent swirling boundary layer is different from a laminar approximation.

Finally, we must reconsider our earlier claim that the upper boundary (or ceiling) of the domain does not have a significant effect on the results. The vortex produced in the simulation with a higher ceiling did in fact have a slightly weaker recirculation zone, a smaller RMW, and a larger ZMW. In other words, the higher ceiling produces a vortex with a smaller internal swirl ratio, S_I. However, we have seen that the maximum average azimuthal wind speed increases with decreasing S_I. Therefore, we must consider the possibility that simulations with larger closed domains will produce tornado-like vortices with higher wind speeds. Investigations on this matter are currently under way, using numerical models with adaptive-mesh-refinement that will make simula-

tions with much larger domains computationally feasible.

Acknowledgments. The authors would like to thank Prof. H. Stone and Prof. G. Flierl for helpful discussions regarding fluid mechanics and vortex dynamics. We would also like to thank Prof. A. Chorin for his extensive advice on numerical modeling, and Dr. M. Minion and Dr. P. Colella for their Godunov method advection routines and their multigrid projection solvers. We are especially grateful to Dr. R. Kupferman for suggesting the methods we used to generate the matrix operators and to enforce higher-order boundary conditions in our analysis of axisymmetric waves in the vortex core. We also gratefully acknowledge the National Energy Research Scientific Computing Center for providing access to the CRAY T3E and providing support for its use. Much of the work for this report was prepared as part of the Ph.D. thesis of D. Nolan while he was a student at Harvard University, during which he was supported by NSF Grants ATM-9216813 and 9623539; after November of 1996, D. Nolan was supported by the Applied Mathematical Sciences Subprogram of the Office of Energy Research, U.S. Department of Energy, under Contract DE-AC03-76SF-00098. B. Farrell was supported by NSF Grant ATM-9216813 and NSF Grant 9623539.

REFERENCES

Barcilon, A. I., 1967: Vortex decay above a stationary boundary. *J. Fluid Mech.,* **27,** 155–175.

Bell, J. B., and D. L. Marcus, 1992: A second order projection method for variable-density flows. *J. Comput. Phys.,* **101,** 334–348.

——, P. Colella, and H. M. Glaz, 1989: A second order projection method for the incompressible Navier–Stokes equations. *J. Comput. Phys.,* **85,** 257–283.

Benjamin, T. B., 1962: Theory of the vortex breakdown phenomenon. *J. Fluid Mech.,* **14,** 593–629.

Burggraf, O. R., K. Stewartson, and R. Belcher, 1971: Boundary layer induced by a potential vortex. *Phys. Fluids,* **14,** 1821–1833.

Chandresekhar, S., 1961: *Hydrodynamic and Hydromagnetic Stability.* Oxford University Press, 652 pp.

Chorin, A. J., 1968: Numerical solution of the Navier–Stokes equations. *Math. Comput.,* **22,** 35–47.

——, 1969: On the convergence of discrete approximations to the Navier–Stokes equations. *Math. Comput.,* **23,** 341–353.

Church, C. R., and J. T. Snow, 1993: Laboratory models of tornadoes. *The Tornado: Its Structure, Dynamics, Prediction, and Hazards,* C. Church et al., Eds., Amer. Geophys. Union, 277–296.

——, ——, G. L. Baker, and E. M. Agee, 1979: Characterisitics of tornado-like vortices as a function of swirl ratio: A laboratory investigation. *J. Atmos. Sci.,* **36,** 1755–1776.

Colella, P., 1990: Multidimensional upwind methods for hyperbolic conservation laws. *J. Comput. Phys.,* **94,** 61–66.

Drazin, P. G., and W. H. Reid, 1981: *Hydrodynamic Stability*. Cambridge University Press, 526 pp.

Emanuel, K. A., 1994: *Atmospheric Convection.* Oxford University Press, 580 pp.

Fiedler, B. H., 1993: Numerical simulation of axisymmetric tornadogenesis in forced convection. *The Tornado: Its Structure, Dynamics, Prediction, and Hazards,* C. Church et al., Eds., Amer. Geophys. Union, 41–48.

——, 1994: The thermodynamic speed limit and its violation in axisymmetric numerical simulations of tornado-like vortices. *Atmos.–Ocean,* **32,** 335–359.

——, 1995: On modelling tornadoes in isolation from the parent storm. *Atmos.–Ocean,* **33,** 501–512.

——, and R. Rotunno, 1986: A theory for the maximum windspeeds in tornado-like vortices. *J. Atmos. Sci.,* **43,** 2328–2340.

Harvey, J. K., 1962: Some observations of the vortex breakdown phenomenon. *J. Fluid Mech.,* **14,** 585–592.

Howells, P. C., R. Rotunno, and R. K. Smith, 1988: A comparative study of atmospheric and laboratory analogue numerical tornado-vortex models. *Quart. J. Roy. Meteor. Soc.,* **114,** 801–822.

Klemp, J. B., and R. B. Wilhelsom, 1978: The simulation of three-dimensional convective storm dynamics. *J. Atmos. Sci.,* **35,** 1070–1096.

Lamb, Sir Horace, 1932: *Hydrodymanics.* Dover, 738 pp.

Lewellen, W. S., 1993: Tornado vortex theory. *The Tornado: Its Structure, Dynamics, Predictions, and Hazards,* C. Church et al., Eds., Amer. Geophys. Union, 19–40.

Lilly, D. K., 1969: Tornado dynamics. NCAR Manuscript 69-117, 39 pp. [Available from NCAR, P.O. Box 3000, Boulder, CO 80307.]

Lugt, H. J., 1989: Vortex breakdown in atmospheric columnar vortices. *Bull. Amer. Meteor. Soc.,* **70,** 1526–1537.

Maxworthy, T., 1973: A vorticity source for large-scale dust devils and other comments on naturally occurring columnar vortices. *J. Atmos. Sci.,* **30,** 1717–1722.

Minion, M. L., 1994: Two methods for the study of vortex patch evolution on locally refined grids. Ph.D. thesis, University of California, Berkeley, 121 pp. [Available from Department of Mathematics, University of California, Berkeley, Berkeley, CA 94720.]

——, 1996: On the stability of Godunov-projection methods for incompressible flow. *J. Comput. Phys.,* **123,** 37–58.

Nolan, D. S., 1996: Axisymmetric and asymmetric vortex dynamics in convergent flows. Ph.D. thesis, Harvard University, 279 pp. [Available from University Microfilm, 305 N. Zeeb Rd., Ann Arbor, MI 48106.]

Peyret, R., and T. D. Taylor, 1983: *Computational Methods for Fluid Flow.* Springer-Verlag, 487 pp.

Rasmussen, E. N., J. M. Straka, R. Davies-Jones, C. A. Doswell III, F. H. Carr, M. D. Eilts, and D. R. MacGorman, 1994: Verification of the Origins of Rotation in Tornadoes: VORTEX. *Bull. Amer. Meteor. Soc.,* **75,** 995–1006.

Rayleigh, Lord, 1880: On the stability and instability of certain fluid motions. *Proc. London Math. Soc.,* **11,** 57–70.

Rotunno, R., 1977: Numerical simulation of a laboratory vortex. *J. Atmos. Sci.,* **34,** 1942–1956.

——, 1979: A study in tornado-like vortex dynamics. *J. Atmos. Sci.,* **36,** 140–155.

——, 1984: An investigation of a three-dimensional asymmetric vortex. *J. Atmos. Sci.,* **41,** 283–298.

Serrin, J., 1972: The swirling vortex. *Philos. Trans. Roy. Soc. London,* **271,** 325–360.

Taylor, G. I., 1923: Stability of a viscous liquid contained between two rotating cylinders. *Proc. Roy. Soc.,* **223A,** 289–343.

Walko, R., and R. Gall, 1986: Some effects of momentum diffusion on axisymmetric vortices. *J. Atmos. Sci.,* **43,** 2137–2148.

Ward, N. B., 1972: The exploration of certain features of tornado dynamics using a laboratory model. *J. Atmos. Sci.,* **29,** 1194–1204.

Wicker, L. J., and R. B. Wilhelmson, 1995: Simulation and analysis of tornado development and decay within a three-dimensional supercell thunderstorm. *J. Atmos. Sci.,* **52,** 2675–2703.

Wilson, T., and R. Rotunno, 1986: Numerical simulation of a laminar end-wall vortex and boundary layer. *Phys. Fluids,* **29,** 3993–4005.

Wurman, J., J. M. Straka, and E. N. Rasmussen, 1996: Fine-scale doppler radar observations of tornadoes. *Science,* **272,** 1774–1777.